Faculty and Researchers   Faculty and Researchers' Publications

2019-03

A Variational Method for Sea Ice Ridging in Earth System Models

Roberts, A.F.; Hunke, E.C.; Kamal, S.M.; Lipscomb, WH; Horvat, C.; Maslowski, W.

Quarterly Journal of the
Royal Meteorological Society   RMetS

Assessing the mechanisms governing the daytime evolution of marine stratocumulus using large-eddy simulation

Lucas A. McMichael[1] | David B. Mechem[1] | Shouping Wang[2] | Qing Wang[3] |
Yefim L. Kogan[4] | João Teixeira[5]

[1]Department of Geography and Atmospheric Science, University of Kansas, Lawrence, Kansas
[2]Naval Research Laboratory, Monterey, California
[3]Department of Meteorology, Naval Postgraduate School, Monterey, California
[4]NorthWest Research Associates, Redmond, Washington
[5]Jet Propulsion Laboratory, California Institute of Technology, Pasadena, California

Correspondence
Lucas A. McMichael, Department of Geography and Atmospheric Science, University of Kansas, Lawrence, KS 66045.
Email: mcmichael@ku.edu

Large-eddy simulation (LES) output for a case of thin stratocumulus off the coast of California is examined in a mixed-layer analysis framework to identify the specific mechanisms responsible for governing the evolution of the cloud system. An equation for cloud-base height tendency isolates the individual cloud-modulating mechanisms that control the evolution of boundary-layer liquid-water static energy (S_l) and total water mixing ratio (q_T). With a suitable spin-up procedure, the control simulation performs admirably compared with observed estimates of liquid water content, vertical velocity variance, and radiative fluxes sampled during an aircraft field campaign. Investigation of the cloud response to various environmental forcing scenarios was addressed through a suite of sensitivity simulations, including variations in subsidence velocity, surface fluxes, wind shear near the inversion, and radiative forcing. In the control simulation, rising cloud-base tendencies are associated with entrainment warming/drying and short-wave absorption, whereas lowering cloud-base tendencies are driven by long-wave cooling. Even in the presence of substantial afternoon solar heating, entrainment fluxes remained active. The thin cloud demonstrated unexpected resiliency, with mixed-layer analysis indicating that, as the short-wave flux decreases later in the afternoon, the relative contribution of long-wave cooling often becomes large enough to offset entrainment warming/drying and result in a reversal of cloud-base tendency. The evolution of cloud-base tendency is found to be insensitive to the net radiative flux divergence for most of the simulations (liquid water path ranging from ~10–50 g/m^2). Error analysis in comparison with LES S_l and q_T budgets suggests that our method of entrainment flux calculation could be improved by a more complete understanding of entrainment-layer physics.

KEYWORDS

afternoon, large-eddy simulation, marine, mixed-layer model, stratocumulus

1 | INTRODUCTION

Stratocumulus clouds are the dominant cloud type on Earth, covering approximately 23% of the ocean surface on average (Wood, 2012). Stratocumulus clouds typically coincide with regions of statically stable lower-tropospheric conditions, which commonly occur over cold oceans and in regions of large-scale subsidence, such as the descending branches of the Hadley and Walker circulations (Klein and Hartmann, 1993). Because of the combination of large areal cloud coverage and high albedo (Chen *et al.*, 2000), marine stratocumulus plays an important role in the global radiation budget. Minor differences in cloud albedo and cover can have major implications on radiation budgets, comparable with those caused by increasing greenhouse gas concentrations (Hartmann and Short, 1980). Understanding the processes governing the evolution of stratocumulus is crucial in representing the global radiation budget accurately in Earth system models (ESMs).

The diurnal cycle of stratocumulus clouds is well documented, with a typical peak in coverage and thickness during the early morning hours (Rozendaal *et al.*, 1995). Maximum drizzle production also coincides with the early morning peak in stratocumulus thickness (Comstock *et al.*, 2004; Sears-Collins *et al.*, 2006; Leon *et al.*, 2008; Burleyson *et al.*, 2013). Burleyson and Yuter (2015) determined that the diurnal cycle of cloud fraction was dependent on the region being observed, with the northeast (NE) Pacific showing the lowest amplitude variability and slowest rates of dissipation, in contrast to the southeast (SE) Pacific and SE Atlantic. The earliest cloud break-up times normally occur near the edges of the stratocumulus deck and correspond to lower values of cloud fraction (Burleyson and Yuter, 2015). The fastest rates of dissipation typically occur around 1200 h local time (LT), with a gradual slowing of the dissipation rate until ~1500–1600 h LT, when short-wave fluxes decrease and the cloud begins to recover (Burleyson and Yuter, 2015).

Similarly to night-time conditions, daytime stratocumulus dynamics remain convectively driven by long-wave cooling at the cloud top, but long-wave cooling is moderated by solar absorption (Caldwell *et al.*, 2005; Wood, 2012), which is dependent upon cloud optical depth, droplet size, and the solar zenith angle (Stephens, 1978). By limiting negative buoyancy production near the cloud top, solar absorption reduces entrainment rates through a decrease in boundary-layer turbulent kinetic energy (TKE: Bretherton and Wyant, 1997). In the absence of stronger turbulent eddies, subcloud moisture is less able to be transported into the cloud layer, which as a result warms and dries with respect to the subcloud layer. This asymmetry is reflected in downward-moving parcels reaching their lifted condensation levels (LCLs) at a higher level than the LCL for surface-based updrafts (Stevens *et al.*, 1998; Wood, 2012; de Roode *et al.*, 2016). The dissimilarity of the LCLs of upward- and downward-moving parcels is manifested as negative buoyancy fluxes near the cloud base and a decoupling of the boundary layer into distinct cloud and subcloud-layer circulations (Nicholls and Leighton, 1986). In thicker clouds, drizzle can also promote decoupling by evaporating in the subcloud layer, cooling and moistening it, and thereby stabilizing the boundary layer. The decoupled, conditionally unstable (as opposed to well-mixed) boundary layer can occasionally support isolated cumulus development (Stevens *et al.*, 1998), which can help to maintain the stratocumulus through an injection of subcloud-layer moisture (Chung *et al.*, 2012). However, these cumulus clouds are associated with vigorous updrafts that may generate enhanced entrainment rates and a gradual dissipation of the overlying stratocumulus (de Roode *et al.*, 2016).

There have been relatively few attempts to examine daytime tendencies in cloud properties comprehensively under a wide range of environmental forcing scenarios to explore the dominant mechanisms responsible for cloud evolution. One notable attempt at quantifying the conditions governing cloud break-up is the cloud-top entrainment instability (CTEI) criterion (Randall, 1980; Deardoff, 1980), which was based solely on the strength of cloud-top moisture and energy gradients. Although the CTEI criterion has been found lacking (Stevens *et al.*, 2003), in part because of its inability to account for larger-scale processes such as surface latent heat fluxes or radiative cooling (Yamaguchi and Randall, 2008), it attempts to address an important question: what are the main drivers promoting changes in cloud properties under varying environmental forcings?

Large-eddy simulations (LES) explicitly resolve the eddies responsible for the majority of the energy and moisture transport in the boundary layer (Lewellen and Lewellen, 1998) and provide a valuable tool for testing hypotheses regarding boundary-layer clouds. Stratocumulus transitioning from solid to broken cloud regimes in the daytime hours is particularly sensitive to changes in the entrainment rate, and realistic model representations of stratocumulus depend on an accurate portrayal of cloud-top entrainment (Stevens *et al.*, 2005). Although the utility of LES lies in its ability to resolve much of the energy containing turbulence, the entrainment rate has been found to be sensitive to the more equivocal components, such as subgrid-scale mixing and the choice of numerical advection scheme (Stevens *et al.*, 2005). Lewellen and Lewellen (1998) discussed the importance of a wide range of scales responsible for determining the amount of radiative cooling experienced by the cloud system, from the local thermal and moisture gradients to the ability of larger-scale eddies to mix directly radiatively cooled air with warm inversion air. Despite the aforementioned uncertainties, Sandu and Stevens (2011) were able to reproduce the main features of non-steady-state stratocumulus-to-cumulus transitions (SCTs) in comparison with observations/reanalysis, which is a testament of the utility of LES in modeling transient cloud systems. Chung *et al.* (2012) also exhibit the ability to represent the SCT within the LES framework. Ghonima *et al.* (2016) used a combination of LES and mixed-layer models (MLMs) and found that the controlling factors dictating stratocumulus lifetime over coastal land regions were the cloud-top entrainment rate, the Bowen ratio at the surface, and the strength of cold-air advection induced by the daytime sea-breeze circulation. However, the surface forcing mechanisms modulating daytime stratocumulus processes over the cool ocean surface are different, with latent heat fluxes often dominating the sensible heat fluxes (small Bowen ratios).

In spite of the previously discussed mechanisms leading to cloud thinning during the daylight hours, stratocumulus clouds are generally resilient to perturbations of cloud water, owing to cloud–radiation–turbulent-entrainment feedback (Zhu *et al.*, 2005). This feedback arises from the relationship between cloud thickness and entrainment rate, with thicker clouds promoting stronger entrainment of warm, dry air through stronger evaporative cooling potential and increased TKE, whereas thinner clouds reduce entrainment as a result of having a lower liquid water content (Wood, 2012). Additionally, Sandu *et al.* (2008) found that, in cases
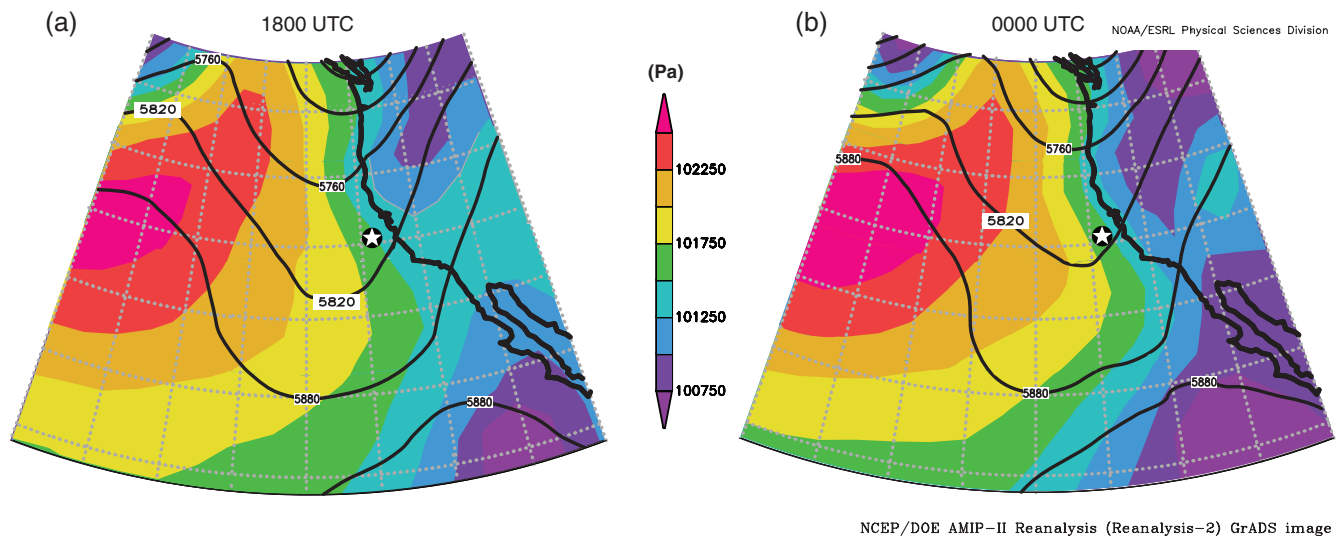
FIGURE 1 500-mb geopotential heights (60 m height intervals) overlaid on mean sea-level pressure (Pa) for (a) 1800 UTC on August 31, 2012 and (b) 0000 UTC on September 1, 2012. The star denotes the initial location of the model domain. NCEP Reanalysis 2 data provided by the Physical Sciences Division, Earth System Research Laboratory, NOAA, Boulder, Colorado, USA, from their website at http://www.esrl.noaa.gov/psd/

where afternoon stratocumulus drizzle was not strong enough to reach the surface, evaporation below the cloud base resulted in destabilization with respect to the surface, a result echoing earlier studies (Feingold *et al.*, 1996; Jiang *et al.*, 2002). Destabilization from the evaporation of drizzle acts to promote deeper-layer mixing and dampens the susceptibility to decoupling that would normally be anticipated given the short-wave absorption in the cloud layer (Sandu *et al.*, 2008).

Variations in subsidence velocity, radiative flux divergence, surface fluxes, inversion structure, and free tropospheric conditions occur across a wide range of temporal and spatial scales. The interconnectedness of the forcing mechanisms introduces a considerable amount of uncertainty when attempting to disentangle the relative importance of the individual mechanisms of dissipation (Caldwell *et al.*, 2005). While LES provides a way to model nonlinear processes in extraordinary detail, the causal relationships between variables are often difficult, or even impossible, to obtain from examining output alone. This research focuses on reducing the complexity of LES output into a more workable format, where conclusions can be drawn on specific mechanisms that govern the evolution of thin cloud systems during the afternoon. By utilizing mixed-layer theory and an extension of a cloud-base tendency equation first developed by Wood (2007), in addition to budget equations for energy and moisture, we can attribute changes in the cloud-base/thickness tendencies to specific mechanisms. The extensive examination of the cloud response to various environmental conditions is explored using a mixed-layer framework, where all mixed-layer variables are obtained from LES output. The mixed-layer approach, in conjunction with traditional analysis of LES output, allows us to draw conclusions about the fundamental behavior of thin, marine clouds. In section 2, we discuss the case study and observations, model description and set-up, mixed-layer model formulation, and mixed-layer

budget uncertainties. In section 3, we present a control simulation synopsis and results for the various environmental forcing scenarios. In section 4, we summarize our findings and provide our conclusions.

2 | METHODOLOGY

2.1 | UPPEF RF01 observations

All simulations are based on observations collected during the first research flight (RF01) of the Unified Physical Parameterization for Extended Forecast (UPPEF) field campaign on August 31, 2012. At 1800 UTC (Figure 1), a nearly neutrally tilted 500-mb trough was slowly propagating eastward and by 0000 UTC it was aligned with the northern California coast. Near the surface, pressures were falling over the Western USA (likely as a result of surface heating), while the subtropical high was gradually spreading eastward (Figure 1). An associated tightening of the zonal pressure gradient occurred at the surface over the course of the afternoon, with winds generally out of the north/northwest in the vicinity of our analysis domain.

Figure 2 displays hourly visible satellite imagery analysis from *GOES-15* and a depiction of a much larger version of our Lagrangian model domain (moving with the mean flow) to illustrate the macroscopic evolution of the stratocumulus deck. The Center for Interdisciplinary Remotely-Piloted Aircraft Studies (CIRPAS) Twin Otter aircraft departed from the Marina Airport at approximately 1900 UTC (local noon) and sampled the coastal environment during its 5-hr long flight. The Twin Otter paid special attention to a sharp clear/cloud boundary in the stratocumulus, which resided on the cool side of a strong sea-surface temperature (SST) gradient (not shown). The SST gradient was oriented from northwest to southeast paralleling the California coast and
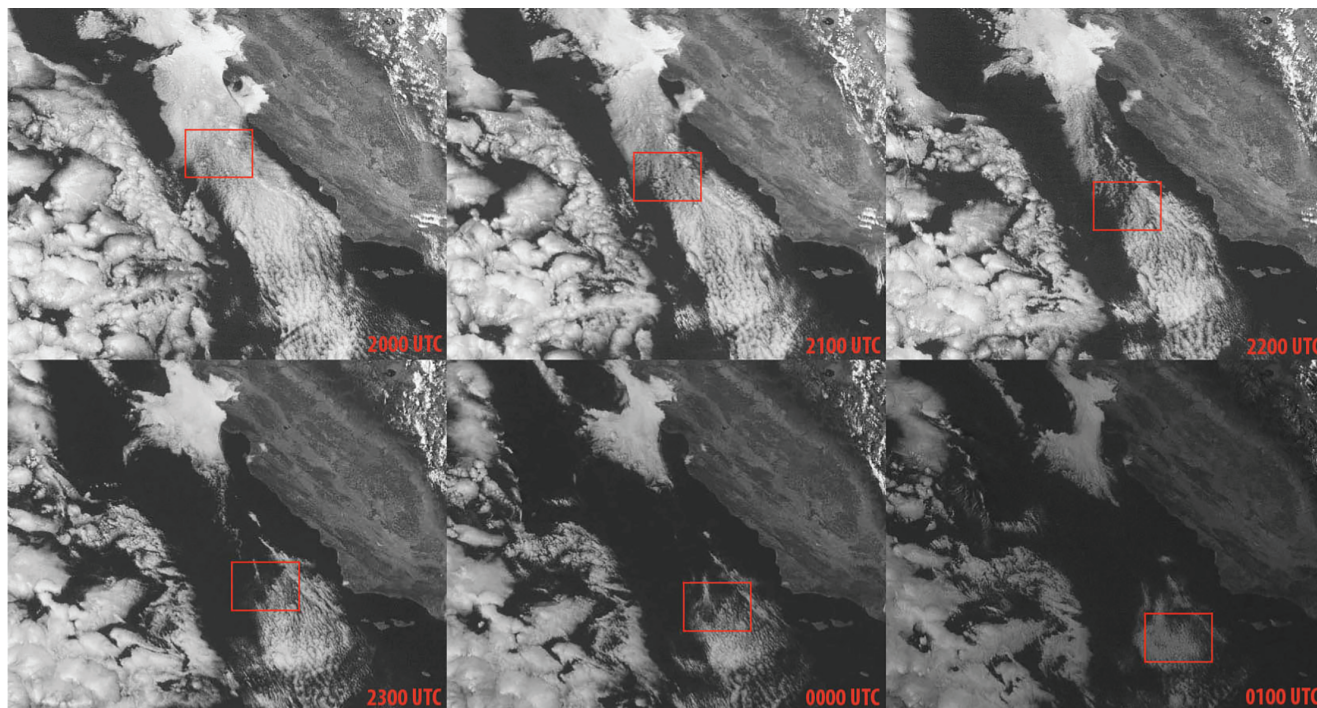
FIGURE 2 *GOES-15* visible satellite imagery at hourly intervals (2000–0100 UTC) on August 31st, 2012. The red box denotes a larger representation of our Lagrangian analysis domain moving at a constant velocity of 13.5 m/s out of the northnorthwest (NNW) (335°)

separated the western periphery of the nearly homogeneous, small horizontal-cell structure (cell size of ~2 km) stratocumulus from a narrow corridor of clear air (Figure 2). The aforementioned stratocumulus deck was approximately 75 nautical miles in width and extended from Cape Mendocino to Santa Barbara, generally ranging from 100–300 m thick. The area west of 125°W featured deep stratocumulus with cell sizes of the order of 50 km, but this western stratocumulus regime was not sampled by the aircraft (Wang *et al.*, 2014). After 2000 UTC, thinning of the coastal stratocumulus deck ensued during the next several hours, extending from Monterey Bay to near Point Conception, with portions of the cloud deck remaining intact to the north and south of these locations, respectively. The satellite imagery in Figure 2 suggests cloud recovery after 2300 UTC as insolation decreases.

The CIRPAS Twin Otter aircraft was equipped with a large suite of instruments. The aircraft gathered horizontal and vertical velocities, absolute humidity using a modified Campbell Scientific fast krypton hygrometer (KH20) and LI-COR 7500 gas analyzer, bulk liquid water content measured with a PVM-100A probe, and ambient temperatures using a Rosemount total temperature sensor. All aforementioned variables were measured at a frequency of 40 Hz. A plethora of particle and drop-size distribution/concentration measurements were made, but they are not examined in this research (Wang *et al.*, 2014). The aircraft also gathered downwelling and upwelling solar irradiance (Kipp and Zonen CM-22 pyranometers), along with upwelling infrared irradiance (Kipp and Zonen CG4 pyrgeometers). The downwelling infrared pyrgeometer was inoperative. All radiation measurements were gathered at a frequency of 1 Hz (Wang *et al.*, 2014).

The focal point of the UPPEFF RF01 was to investigate the differences in surface fluxes between the clear and cloudy regions, which in RF01 coincided with the SST gradient mentioned previously. Much of the flight duration was spent measuring surface/near-surface fluxes and the low-level turbulent structure in proximity to the clear/cloud boundary. Therefore, comparatively little emphasis was given to level legs in the cloud layer and full soundings through the depth of the cloud layer. For this reason, the aircraft data are somewhat limited in representing the evolution of cloud properties over the course of the afternoon. Nevertheless, we strive to incorporate all available measurements to constrain and validate model behavior.

2.2 | LES configuration

Simulations were performed using the System for Atmospheric Modeling (SAM), version 6.10.6 (Khairoutdinov and Randall, 2003). SAM is a non-hydrostatic model that employs the anelastic approximation, which filters acoustic waves. The model was run in traditional LES mode over the ocean surface, assuming horizontally homogeneous surface fluxes across the domain, given that the longitudinal position of the SST gradient varied minimally over the course of the afternoon (Tellado, 2013), and fairly uniform SSTs on the cool side of gradient along the domain trajectory (~286–287 K), as estimated by NASA JPL G1SST data. Surface sensible and latent heat fluxes were prescribed using fluxes measured by the Twin Otter, while surface momentum fluxes were computed according to Monin–Obukhov similarity theory, with a surface roughness height of 0.1 cm (Monin and Obukhov,

1954). The model employs thermodynamic variables of liquid water static energy (S_l) and total water mixing ratio (q_T), which are conserved for moist adiabatic processes. A fifth-order advection scheme (ULTIMATE-MACHO: Yamaguchi *et al.*, 2011) was implemented to limit numerical diffusion and the associated damping of turbulent kinetic energy (TKE). Numerical solutions to the partial differential equations for momentum were solved using the third-order Adams–Bashforth time-differencing method. The CAM3 radiation package (Collins *et al.*, 2006) was used for long- and short-wave radiative fluxes for every model time step (2 s), with a diurnally varying zenith angle. The subgrid-scale turbulence scheme uses a prognostic 1.5-order TKE closure developed by Deardoff (1980), which predicts the TKE using shear and stability profiles and diagnoses eddy diffusivity and dissipation.

Detailed representations of precipitation processes are of little significance in this essentially non-precipitating event, so single-moment (hydrometeor mixing ratio) bulk microphysics was used to increase computational efficiency. This simple microphysics parametrization assumes saturation adjustment to diagnose liquid water content and partitions hydrometeors into precipitating and non-precipitating classes (Kessler, 1969). The LES does not account for cloud droplet sedimentation, which has been found to reduce excessive entrainment (Ackerman *et al.*, 2004; Bretherton *et al.*, 2007), but we speculate this mechanism to be less important for our case, with exceptionally low liquid water contents (and hence small droplets) and a LWP 5–20 times smaller than the clouds examined in Ackerman *et al.* (2004). A vertically refined grid of 5 m in the 600–1,000 m layer, similar to that used by Caldwell and Bretherton (2009), is used to minimize computational cost and attempt to simulate cloud-top entrainment accurately. The vertical grid is approximately 21 km (168 grid levels) in depth in order to model downwelling radiative fluxes at the top of the boundary layer. A simulation using a 5-m vertical grid spacing throughout the entire depth from 0–1,500 m was nearly indistinguishable from the stretched grid run, providing confidence in our stretched vertical grid structure. Our configuration, along with several other studies, has shown that entrainment is rather unresponsive to horizontal grid spacing (Lewellen and Lewellen, 1998; Stevens *et al.*, 1999), although Stevens *et al.* (1999) determined the insensitivity may stem from the sub-grid scale (SGS) formulation. Given the inherent uncertainties regarding numerical/SGS schemes, a fairly coarse horizontal grid of 35 m was employed. The model consists of 128×128 grid points in the horizontal, equating to a 4.48×4.48 km^2 horizontal grid initially centered on (35.9°N, 123.4°W). Boundary conditions are doubly periodic and the vertical damping of waves in the top 30% of the domain was accomplished by a Rayleigh sponge layer. All simulations are run for 6 hr, and statistics are computed using 30-min averages.

2.3 | Model initialization and spin-up procedure

Low-altitude (below 1,200 m) soundings for model intial conditions were derived from the 7-min aircraft descent from 2113–2120 UTC (Figure 3, red line labeled 2117 UTC), which sampled the thin cloud layer on the cool side of a strong SST gradient (the warm side was predominantly cloud-free). The aircraft soundings in Figure 3 showed the presence of a strong inversion (potential temperature and moisture jumps of ~10 K and ~7 g/kg, respectively) near 900 m and conditions supportive of coastal stratocumulus. Aircraft observations indicate initial stratification in the water-vapor mixing ratio profile, with a surface value of 8.75 g/kg and an inversion base value of 7.25 g/kg. The observed potential temperature profile was nearly constant over the boundary layer, with an inversion depth of approximately 25 m and a cloud-top jump of 9.5 K separating the boundary layer from the free troposphere. Vertical profiles of horizontal velocities revealed minimal shear in the *u*-component and evidence of a moderate coastal jet in the *v*-component, with a strong northerly flow (7–10 m/s) in the boundary layer. Model initial conditions employ an idealized treatment of the aircraft-derived initialization profiles of potential temperature, water-vapor mixing ratio, and horizontal velocities shown in Figure 3 (black lines). Owing to low liquid water contents, observed potential temperature and water-vapor mixing ratio profiles were treated as liquid potential temperature (θ_l) and total water mixing ratio (q_T). Atmospheric moisture and temperature profiles above 1,200 m were estimated using a blend of the 1200 and 0000 UTC Oakland (KOAK) soundings. Synoptic forcing was weak and the atmosphere nearly barotropic above the boundary layer, so the winds above 1,200 m were assumed to be constant, with *u* and *v* components of 5 and −4 m/s, respectively. Surface fluxes over the cool, cloudy side of the SST gradient were prescribed according to aircraft observations, with no sensible heat flux and a small latent heat flux of 4.45 W/m^2.

All simulations assume a Lagrangian framework, justified by the modest vertical shear in the upper boundary layer and weak moisture and temperature gradients along the trajectory of our model domain, so large-scale advective tendencies are deemed unnecessary in our idealized representation of the case. Furthermore, the small spatial variation of SST gradient (Tellado, 2013) reinforces our confidence that the model domain remains on the cool side of the SST gradient and avoids any significant baroclinic influences. Estimates of large-scale vertical motion are based on the inner, 5-km nest of a doubly nested operational run of the Coupled Ocean–Atmosphere Mesoscale Prediction System (COAMPS: Hodur, 1997) conducted in support of the field campaign (not shown). We simplified the COAMPS vertical motion profile to decrease linearly from 0 cm/s at the surface to −1.0 cm/s at 900 m, remaining constant up to a height of 6 km. Above 6 km, subsidence velocities decrease linearly to 0 cm/s by 10 km.
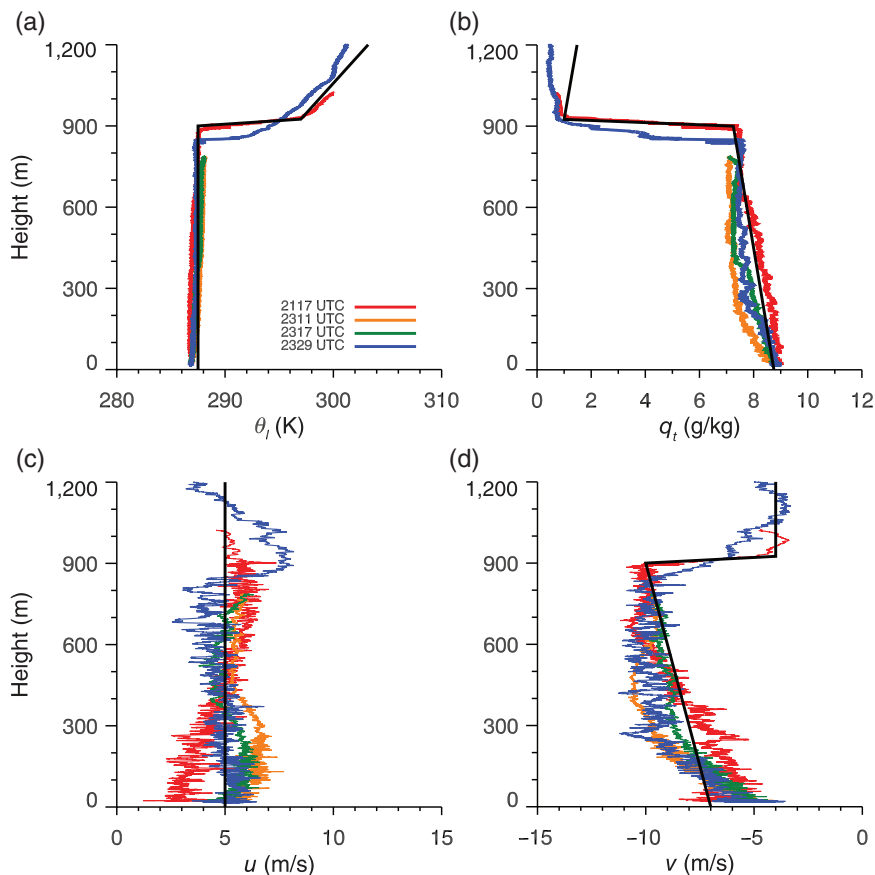
FIGURE 3 Idealized profiles (black lines) used for model initialization with observed aircraft soundings in the vicinity of the primary aircraft sounding (2117 UTC) superimposed. (a) Liquid potential temperature (θ_l), (b) total water mixing ratio (q_T), (c) u-velocity component, and (d) v-velocity component

By the addition of small-amplitude random noise to the model's initial values over the lowest vertical levels, the initial quiescent state is perturbed and turbulence develops. The time it takes this perturbed state to reach a dynamic equilibrium is referred to as the model spin-up time. This particular non-steady-state stratocumulus case presents several challenges, since the model variables must arrive at a post-spin-up state that represents observed thermodynamic and dynamic structures. In other words, by the time the spin-up process is complete, ideally, the thermodynamic and dynamic fields must be well-matched to our available observations. Our SAM configuration has a spin-up time of roughly 1.25 hr. We attempted to find an optimal solution that evolved appropriately, according to aircraft and satellite observations of the case using various methods to increase initial LWP slightly, including negative temperature tendencies in the boundary layer, reducing subsidence, employing only long-wave radiation, and altering surface fluxes during the spin-up period.

2.4 | Mixed-layer budget formulation

LES results are examined using a mixed-layer budget analysis of moisture, energy, and mass, employing the moist-adiabatically conserved variables of q_T and S_l predicted by SAM. q_T is the sum of water vapor (q_v) and liquid water mixing ratios (q_l) and $S_l = C_p T + gz - L_v q_l$, where T is

temperature and g is acceleration due to gravity. The heat capacity of dry air at constant pressure C_p and L_v are considered constants, with values of $1004 \, \mathrm{J \, kg^{-1} \, K^{-1}}$ and $2.5 \times 10^6 \, \mathrm{J/kg}$, respectively. A mixed-layer budget framework provides a unique avenue for exploring the role of different mechanisms governing the evolution of the cloud field through cloud-base and cloud-thickness tendencies. We first develop mixed-layer budgets of q_T and S_l by employing a method similar to Caldwell *et al.* (2005), who partitioned energy and moisture budgets into individual forcing terms, including surface fluxes, entrainment fluxes, radiative flux divergence, precipitation rates at the surface, net latent heating terms, and horizontal advection. The MLM framework is then extended using approaches similar to those of Wood (2007) and Ghonima *et al.* (2016) to yield a budget equation for cloud-base tendency in order to determine the relative importance of each budget term in regulating cloud-base/thickness tendency. Cloud-base tendency was the preferred analysis method in this particular case, because of large variations of inversion-base height (z_i). In many of these runs, the LWP tendency is dominated by the inversion height tendency, since the LWP scales as the square of the cloud thickness. Instead, we are interested in changes to the boundary-layer saturation conditions (profiles of mixing ratio and saturation mixing ratio) from mechanisms governing the evolution of q_T and S_l budgets (for example, entrainment or radiation) that are

discernible from changes in inversion height. The cloud-base tendency can be transformed into cloud-thickness tendency by incorporating the inversion height tendency, which must be done to ascertain the cloud evolution appropriately in the presence of a non-stationary inversion.

The mixed-layer moisture budget equation determines the time tendency of q_T as a function of the individual forcing terms that act as controls on boundary-layer moisture (Equation 1). Dry-air entrainment of free tropospheric air is one possible sink of boundary-layer moisture. The rate at which free tropospheric air is entrained into the boundary layer is given by the entrainment flux, $\overline{(w'q_T')}_e$, and is commonly parametrized as the product of entrainment rate, w_e, and Δq_T, which represents the cloud-top jump (moisture gradient) between the cloud layer and the free troposphere. While the entrainment term represents a sink of boundary-layer moisture originating from the upper boundary, the surface moisture flux term ($q_{Tsfc}/(\rho L_v)$) accounts for changes attributable to the surface boundary condition, where ρ represents the mean boundary-layer air density and L_v is the latent heat of vaporization. As mentioned previously, surface fluxes are prescribed in the model and remain constant for the duration of the simulation. Another possible sink in the moisture budget is the removal of liquid water through precipitation, given by the surface precipitation rate P_0. All the previously mentioned terms are divided by the boundary-layer depth (z_i), which instantaneously distributes moisture changes throughout the boundary layer. The final moisture source/sink is the mean horizontal moisture advection term through the depth of the boundary layer ($-\mathbf{v} \cdot \nabla_h q_T$).

$$\frac{\partial q_T}{\partial t} = \frac{\overline{(w'q_T')}_e + \frac{q_{Tsfc}}{\rho L_v} + P_0}{z_i} - \overline{\mathbf{v} \cdot \nabla_h q_T} \quad (1)$$

The mixed-layer energy budget is similar to the moisture budget, but includes several additional terms and has units of m^2/s^3. The time tendency of S_l is determined by five forcing terms shown in Equation 2. The rate at which dry, warm free tropospheric air is entrained into the boundary layer is represented by $\overline{(w'S_l')}_e$, where, again, this is commonly parametrized by the flux-jump relation ($w_e \Delta S_l$). Surface energy sources are accounted for through the sensible heat flux and given by (S_{lsfc}/ρ). The energy is also altered through radiative heating/cooling, and the net radiative flux divergence is depicted by ($-R_h + R_0$), where R_h is the net radiative flux at the cloud top and R_0 is the net radiative flux at the surface. The net radiative flux divergence was quantified simply by determining the difference in net radiative fluxes from 2D radiation streams at the nearest index of inversion-base height and the first model grid level. Additionally, energy can be added through net latent heating, which is directly proportional to the surface precipitation rate and is denoted by $L_v P_0$. Again, the first four terms are divided by the depth of the boundary layer h. The final term in the energy budget

is the mean horizontal advection of S_l in the boundary layer ($-\overline{\mathbf{v} \cdot \nabla_h S_l}$).

$$\frac{\partial S_l}{\partial t} = \frac{\overline{(w'S_l')}_e + \frac{S_{lsfc}}{\rho} - \frac{R_h}{\rho} + \frac{R_0}{\rho} + L_v P_0}{z_i} - \overline{\mathbf{v} \cdot \nabla_h S_l} \quad (2)$$

In this framework, the mass budget can be employed as the entrainment closure. The entrainment rate (w_e) is obtained as a residual of cloud-top evolution (Equation 3) that is dependent upon the imposed large-scale vertical velocity at the cloud top ($w(z_i)$), advection of cloud-top heights ($-\mathbf{v} \cdot \nabla z_i$), and time tendency of the inversion height ($\partial z_i/\partial t$) (Caldwell and Bretherton, 2009). The inversion height was calculated by taking the vertical derivative of the liquid potential temperature profile (θ_l) and interpolating linearly to a threshold value of 0.05 K/m (which corresponds to a 0.25 K increase over 5 m). Three-dimensional output was used to determine the boundary-layer depth column by column, with cloudy and noncloudy columns considered and averaged horizontally across the domain. As mentioned in Stevens (2006), our mass budget formulation assumes that the turbulence is limited to the boundary layer and mass fluxes out of the boundary layer are not permitted (or accounted for). Since inversion base heights were evaluated from LES output and the advection of cloud-top heights were neglected in our Lagrangian framework, entrainment rate is a relatively straightforward residual calculation, given our mass budget (Equation 3).

$$\frac{\partial z_i}{\partial t} + \mathbf{v} \cdot \nabla z_i = w_e + w(z_i) \quad (3)$$

Although trivial theoretically, the computational accuracy of z_i is dependent upon the ability to correctly and consistently identify the inversion base in the model output and the vertical grid spacing from which the inversion base is estimated (5 m in this case). While inversion-base heights were calculated using θ_l profiles (less stratified than q_T profiles), q_T profiles were used to compute inversion-top heights due to a more distinct boundary between the inversion layer and the free troposphere. The difference between these two aforementioned heights was computed using 3D LES output and then averaged across the model domain to estimate cloud-top jumps/inversion stability in S_l and q_T. The flux-jump relation discussed previously as the product of the entrainment rate and the cloud-top gradient assumes a zero-order discontinuity in standard mixed-layer theory (Nicholls, 1984); however, this is a substantial source of uncertainty in our mixed-layer budgets, due to finite inversion-layer thicknesses on the order of 30 m. Despite the limitations of the zero-order jump model, knowledge of cloud-top jump magnitudes and entrainment rates provides helpful metrics for rationalizing mixed-layer model behavior.

Utilizing resolved entrainment fluxes from the LES provides an alternative way to estimate the cloud-top entrainment flux directly without assuming a zero-order discontinuity or neglecting any upward mass flux that may occur in isolated cumulus updrafts. Several methods of estimating entrainment
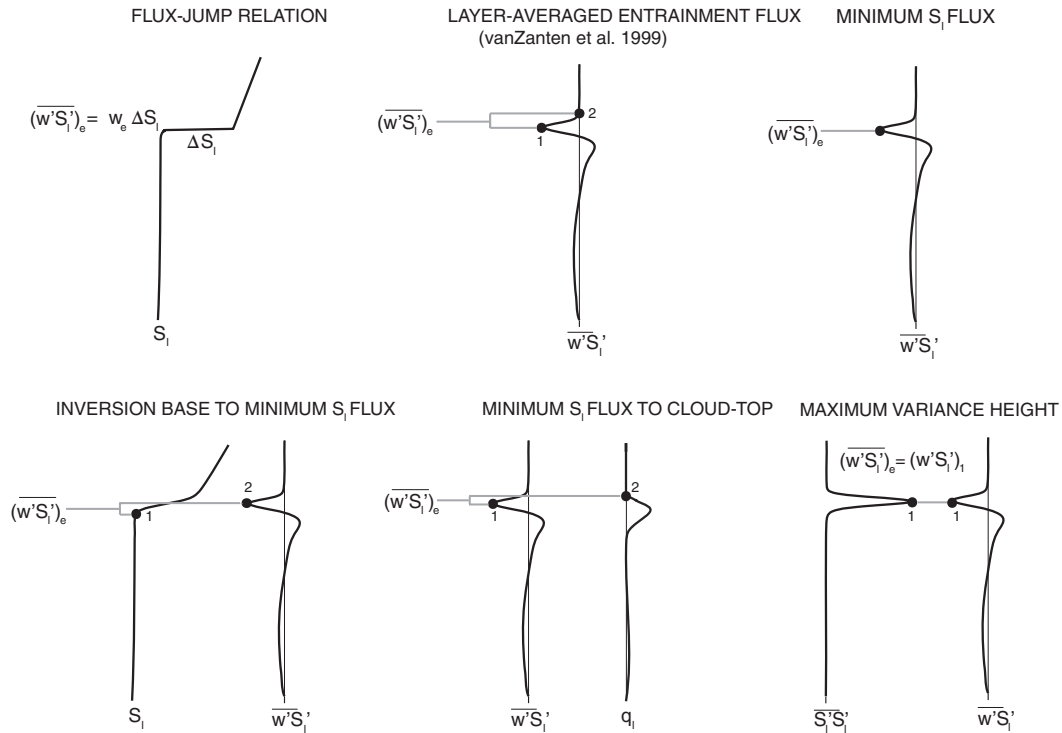
FIGURE 4 Various methods for calculating domain-averaged entrainment fluxes. Flux averages were computed between points 1 and 2. Indices obtained through these methods were applied to q_T flux profiles. The preferred method used for MLM budget analysis is shown at the bottom left

fluxes from the explicit representation of S_l and q_T flux profiles were attempted, to represent best the actual entrainment flux at the top of the boundary layer. Mean boundary-layer quantities of S_l and q_T in the LES were weighted by density and vertical grid spacing. Using the first-order jump model established by VanZanten *et al.* (1999) for convective boundary layers (or very diffuse inversion layers), the entrainment flux was first calculated from the S_l flux profile. The S_l flux profile contains a pronounced minimum near the cloud top associated with warm, dry air entrainment. The entrainment flux is computed as the average from the S_l flux minimum to where the flux approaches zero at a higher altitude (VanZanten *et al.*, 1999). The height indices representing the entrainment layer were used to solve for the q_T entrainment flux in the same manner. Additional methods of entrainment-flux estimation include the minimum S_l flux in the cloud, a layer average from the inversion base to the S_l flux minimum (preferred method; bottom left panel of Figure 4), a layer average from the S_l flux minimum to the top of the cloud, and determining height indices from maximum q_T and S_l variances. Figure 4 illustrates the different entrainment-flux estimation methods and the performance and limitations of the various methods are discussed in section 2.5.

An equation for cloud-base tendency can now be derived by applying the chain rule on q_T and S_l and was expressed in Wood (2007) as Equation 4, where z_{cb} is cloud-base height. This relationship between cloud-base tendency and the moisture and energy budgets requires two additional equations relating cloud-base changes to changes in q_T (Equation 5) and S_l (Equation 6). Equation 5 presents the

relationship between changes in cloud base and changes in q_T, with R_d and R_v being the gas constants of dry and moist air and T_{cb} being the temperature of the cloud base. $\bar{q}_T$ in Equation 5 represents the mean boundary-layer value derived from the LES profile. Heat content is assumed to stay constant and a detailed derivation of Equation 5 can be found in Wood (2007), as well as Ghonima *et al.* (2015).

The cloud-base response to changes in S_l is assumed to occur at constant moisture content and the relation is given by Equation 6, which was developed by Ghonima *et al.* (2015) to bring the original Wood (2007) formulation of cloud-base tendency into agreement with the LWP tendency equation derived in Van der Dussen *et al.* (2014). The original Wood (2007) formulation failed to represent the addition/removal of heat with the use of the dry adiabatic lapse rate and only accounted for the cloud base being a function of temperature, neglecting its dependence on pressure (Ghonima *et al.*, 2015). The amendments made in Ghonima *et al.* (2015) were found to improve the Wood (2007) response to changes in heat content by approximately 22%. Both Equations 5 and 6 are relatively constant over short time-scales and in the absence of significant moisture or temperature advection.

$$\frac{dz_{cb}}{dt} = \frac{\partial z_{cb}}{\partial q_T}\frac{\partial q_T}{\partial t} + \frac{\partial z_{cb}}{\partial S_l}\frac{\partial S_l}{\partial t} \tag{4}$$

$$\frac{\partial z_{cb}}{\partial q_T} = -\frac{R_d T_{cb}}{g\bar{q}_T}\left(\frac{L_v R_d}{C_p R_v T_{cb}} - 1\right)^{-1} \tag{5}$$

$$\frac{\partial z_{cb}}{\partial S_l} = \frac{1}{g}\left(1 - \frac{C_p R_v T_{cb}}{R_d L_v}\right)^{-1} \tag{6}$$

Substituting Equations 2, 3, 5, and 6 into 4 yields an equation for cloud-base tendency (Equation 7). In Equation 7, we have substituted the LES-derived entrainment fluxes (written in standard flux notation) for the flux-jump relation, since this is the preferred method of calculation in this study. Once cloud-base tendencies are calculated from the model, the individual contribution of each budget term to cloud-base height is analyzed and discussed. Net cloud-base tendencies are then compared with LES cloud-base tendencies computed from 3D output using a liquid water content threshold of 0.01 g/kg. All cloudy columns (value of at least 0.01 g/kg) were averaged horizontally to arrive at a mean cloud-base height. All budget analyses were performed over the 2–4 and 4–6 hr periods to avoid spin-up contamination.

$$
\begin{aligned}
\frac{dz_{cb}}{dt} = &-\frac{R_d T_{cb}}{g \bar{q}_T} \left(\frac{L_v R_d}{C_p R_v T_{cb}} - 1 \right)^{-1} \\
&\times \left(\frac{\overline{(w' q_T')}_e + \frac{q_{Tsfc}}{\rho L_v} + P_0}{z_i} - \mathbf{v} \cdot \nabla_h q_T \right) \\
&+ \frac{1}{g} \left(1 - \frac{C_p R_v T_{cb}}{R_d L_v} \right)^{-1} \\
&\times \left(\frac{\overline{(w' S_l')}_e + \frac{S_{lsfc}}{\rho} - \frac{R_h}{\rho} + \frac{R_0}{\rho} + L_v P_0}{z_i} - \mathbf{v} \cdot \nabla_h S_l \right)
\end{aligned}
\tag{7}
$$

2.5 | Mixed-layer budget uncertainties

The mixed-layer assumption naturally assumes the boundary-layer remains well-mixed, and departures from the well-mixed state are manifested as errors in the mixed-layer model budgets. In the LES, stratification is often evidenced by negative buoyancy fluxes near cloud base, or a significant minimum in cloud-base vertical velocity variance (Bretherton and Wyant, 1997; Stevens et al., 2005). Afternoon stratocumulus clouds are susceptible to decoupling from solar absorption (Albrecht et al., 1988) and the uneven distribution of buoyancy flux throughout the boundary layer, with maximum values of buoyancy located in the cloud resulting in a relative minimum near cloud base (Bretherton and Wyant, 1997). Despite afternoon conditions that often support decoupling, small latent heat fluxes over the cool ocean surface limited the stratification in the control run, and the boundary layer was able to remain relatively well-mixed. Deviations from the model-derived cloud-base tendency arise primarily from the disproportionate warming and drying of the cloud layer, violating the assumption in Equation 7 of evenly distributing the fluxes throughout the boundary layer. However, even in cases with substantial departures from a mixed-layer state, knowledge of LES q_T and S_l tendencies provide valuable insights into MLM budget performance.

Even though the LES provides explicit representation of entrainment fluxes it remains difficult to calculate the MLM entrainment flux. The calculation of entrainment fluxes

presents an additional source of uncertainty, because our case clearly deviates from standard mixed-layer theory, with a diffuse inversion and cloud tops that do not coincide perfectly with the inversion base. Traditionally, the entrainment interface is thought to be a sharp transition layer that separates turbulent, saturated air from laminar, unsaturated free-tropospheric air (Randall, 1980). However, Moeng et al. (2005) found that the cloud-top interface and the depth of the boundary-layer mixing are separated by a fairly significant depth (~10–20 m). In order best to represent the nature of the air being entrained into the boundary layer, several ad hoc methods of entrainment flux estimation were attempted, summarized in Figure 4, and the performance of the MLM budgets was gauged by a comparison of LES q_T and S_l budget tendencies, with discrepancies being attributed primarily to the entrainment terms, due to higher confidence in the remaining terms. The relative error (η) was calculated according to Equation 8, with x_{LES} being the LES budget tendency, which was calculated as the time tendency of the mean boundary-layer q_T and S_l, and x_{MLM} being the MLM budget tendency. The absolute error (ϵ) is defined as the numerator in Equation 8. The flux-jump relation (for example, $w_e \Delta q_T$) vastly overestimates entrainment warming and drying, as expected, as the zero-order inversion jump assumption is violated in our case. The layer-averaged entrainment fluxes (VanZanten et al., 1999) grossly underestimate the entrainment warming and drying. Averaging the entrainment fluxes from the minimum S_l flux to the cloud top significantly underestimated entrainment drying, while only slightly underestimating warming. Using the height of the maximum variance performed reasonably well for the S_l budget, but underestimated entrainment drying. The height of the minimum S_l flux produced similar results to our chosen method in the 2–4 hr period, but overestimated entrainment warming in the 4–6 hr period. We found the layer average from the inversion base to the minimum S_l flux to be the most robust method in terms of reconciling with LES budgets.

$$
\eta = \left| \frac{x_{MLM} - x_{LES}}{x_{LES}} \right|
\tag{8}
$$

In general, 2–4 hr mean q_T MLM tendencies indicate too much drying in the MLM, with ~80% of the available simulations (16 total simulations) overestimating drying (Table 1). Only the two latent heat flux sensitivity simulations underestimate drying significantly in the 2–4 hr period. The 4–6 hr mean q_T MLM tendencies suggest underestimation of drying, with ~79% of the simulations (14 simulations had cloud water present during the 4–6 hr period) exhibiting moistening tendencies that are too large compared with the model. There is no clear bias in 2–4 hr mean S_l MLM tendencies; however, the largest relative and absolute errors occur during the 2–4 hr time frame. 4–6 hr mean S_l MLM tendencies underestimate warming ~79% of the time, with only three simulations overestimating warming. The error analysis suggests that our method underestimates the total change in depth

TABLE 1 LES and MLM q_T and S_l tendencies and associated relative η and absolute ϵ errors

	LES Q_T (g kg⁻¹ s⁻¹) ×10⁻⁵	MLM Q_T (g kg⁻¹ s⁻¹) ×10⁻⁵	η (%)	ϵ (g kg⁻¹ s⁻¹) ×10⁻⁶	LES S_l (m² s⁻³)	MLM S_l (m² s⁻³)	η (%)	ϵ (m² s⁻³) ×10⁻³
CONTROL	−1.1	−1.6	45	5	−0.0028	−0.0018	−36	1
	−1.2	−1.1	−8	1	−0.031	−0.033	6	2
NOSUB	−1.9	−2.2	16	3	0.0089	0.0059	−34	3
	−2.0	−1.9	−5	1	−0.015	−0.021	40	6
0.25 cm s⁻¹	−1.7	−2.0	18	3	0.0057	0.0034	−40	2
	−1.8	−1.9	6	1	−0.021	−0.026	24	5
0.5 cm s⁻¹	−1.5	−1.9	27	4	0.0028	0.0018	−36	1
	−1.7	−1.6	−6	1	−0.026	−0.03	15	4
0.75 cm s⁻¹	−1.4	−1.8	29	4	0.0004	−0.0005	−236	0.9
	−1.5	−1.4	−7	1	−0.03	−0.034	13	4
1.25 cm s⁻¹	−0.8	−1.4	75	6	−0.0043	−0.002	−53	2
	−0.7	−0.6	14	1	−0.022	−0.023	5	1
1.5 cm s⁻¹	−0.5	−0.9	80	4	−0.0024	0.002	−184	4
	−0.2	−0.1	−50	1	0.008	0.011	38	3
LHF100	1.7	3.1	82	14	0.008	0.011	38	3
	1.1	2.7	145	16	−0.011	−0.015	36	4
LHF150	3.6	6.1	69	25	−0.0014	0.007	−600	8
	2.5	−5.0	−300	75	−0.0014	0.0069	−593	8
SHF100	3.0	−2.0	−167	50	0.01	0.01	0	0
	–	–	–	–	–	–	–	–
NOSHEAR	−1.1	−1.6	45	5	0.0002	0.0025	1150	2
	−1.1	−1.0	−9	1	−0.021	−0.023	10	2
Directional	−0.6	−1.4	130	8	0.007	0.024	243	17
	–	–	–	–	–	–	–	–
PosVort	−1.0	−1.5	50	5	0.0026	0.008	210	5.4
	−0.4	−0.3	−15	1	−0.002	0.0055	−375	4
NegVort	−0.9	−1.4	56	5	−0.0027	−0.0019	−30	0.8
	−1.0	−1.2	20	2	−0.026	−0.027	4	1
ControlLW	−2.7	−2.7	0	0	−0.024	−0.028	17	4
	−2.0	−1.6	−20	4	−0.04	−0.042	5	2
NOSUBLW	−3.2	−3.0	−6	2	−0.011	−0.021	91	10
	−2.7	−2.2	−19	5	−0.018	−0.028	56	10

Rows with simulation names corresponds to 2–4 hr mean, while unlabeled rows correspond to 4–6 hr mean

of the entrainment layer, with layers that are generally too shallow in the 2–4 hr period and too deep in the 4–6 hr period. We speculate that these errors emerge from increasing static stability of the inversion layer with time and a fundamentally different turbulent structure near the cloud top during the two analysis periods that our current method of entrainment flux calculation is not able to capture fully. Figure 5 illustrates the shift in liquid water content and vertical velocity structure, with earlier time periods having most of the convective motions confined to the cloud layer, while, later on, deeper coherent circulations are able to develop. Also, there are 10 (33% of analysis periods) instances of overestimating one budget variable while underestimating the other, which may suggest that the depth of entrainment layers associated with q_T and S_l may be different. Regardless of the aforementioned uncertainties, the overall magnitudes of the

budget errors are generally small and meaningful deductions can be made from analysis of individual budget terms and comparison with model budget tendencies.

In an attempt to quantify the degree of stratification, a decoupling parameter (ψ) formulated by Park *et al.* (2004) is calculated as the difference of cloud and subcloud $\phi = (q_T, S_l)$ divided by the difference of ϕ just above the inversion layer ($\phi_{\text{invtop}+1}$) and the subcloud layer (Equation 9). Overall, $\psi(S_l)$ is less than $\psi(q_T)$ in both analysis periods and ψ decreases in the 4–6 hr period for both S_l and q_T (Table 2). Absolute errors are generally greater for larger values of ψ, as would be expected given a more substantial deviation from a mixed-layer state.

$$\psi(\phi) = \frac{\phi_{\text{cld}} - \phi_{\text{subcld}}}{\phi_{\text{invtop}+1} - \phi_{\text{subcld}}} \tag{9}$$
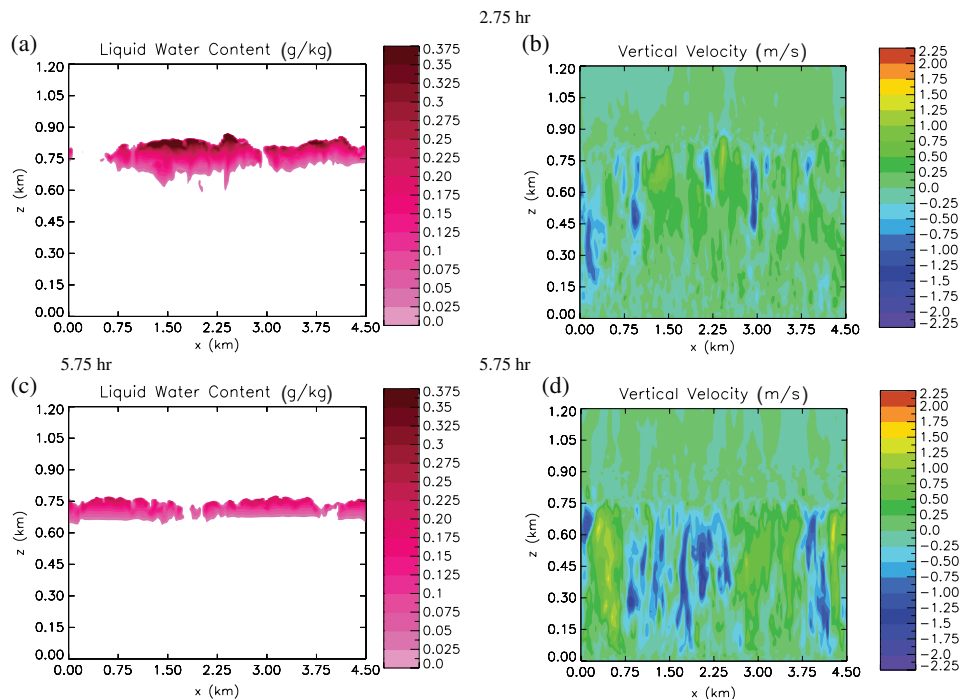
FIGURE 5 2D cross-sections of liquid water content and vertical velocity for the control simulation. (a,b) 2.75 hr and (c,d) 5.75 hr

3 | RESULTS

3.1 | Control simulation overview and initial condition sensitivity

We found that the optimal spin-up procedure included a large-scale negative temperature tendency of 0.75 K/hr for the first 45 min of the simulation. We refer to this as the control simulation. In-cloud vertical velocity variance and liquid water content were increased compared with a baseline simulation with no temperature tendency during the spin-up process by lowering the saturation vapor pressures and were reasonably aligned with aircraft observations (Figure 6). The disparity of the model near-surface vertical velocity variance in comparison with the observations is likely due to the aircraft encountering slightly warmer SSTs as it progressed westward. Modeled downwelling short-wave irradiances both in the cloud and near the surface were consistent with flight observations shortly after the spin-up period, while upwelling long-wave fluxes in the cloud were slightly underestimated by the model (Figure 7). The upwelling short-wave radiative flux in the cloud also matched observations well. Modeled downwelling short-wave irradiance near the surface around 2300 UTC underestimated observed fluxes, but this is likely due to the aircraft sampling at the periphery of the cloud deck, in close proximity to the clear/cloud boundary.

Because the aircraft predominantly sampled conditions below 1,200 m, thermodynamic profiles aloft were specified from KOAK soundings. Sensitivity to the profiles above 1,200 m was tested by simulating a wide range of mid-upper-level temperature profiles (± 5 K from control over the 5–21 km depth), as well as altering free-tropospheric

humidity. In the warm mid-upper-level temperature case, the short-wave radiation budget changes are minor, but downward long-wave radiation fluxes increase, resulting in net radiation increases at the top of the boundary layer. This increase in net radiation in the warm case leads to a slightly thinner cloud (~5–10%) in terms of LWP, while the cold mid-upper-level temperature case did not deviate significantly from the control. Free-tropospheric humidity sensitivity was evaluated through adjusting water-vapor mixing ratios at 1,500 m from 0.5 (drier) to 3.0 (moister) g/kg. Lower free-tropospheric moisture resulted in a similar LWP evolution to the control for the 2–4 hr period, but began to dissipate at a faster rate during the 4–6 hr period. Higher free-tropospheric moisture lowered LWP by ~5–20% for most of the simulation, but ended near the control LWP. Overall, sensitivity to free-tropospheric moisture is minimal, because of higher moisture content reducing drying by entrainment and lower moisture content increasing long-wave and evaporative cooling efficiency, thereby increasing entrainment (Wood, 2012).

The control simulation exhibited a slowly diminishing LWP after spin-up, with a reduction of 7.1 g/m^2 over the course of the simulation (Figure 8). Cloud fraction remained near unity and never fell below 0.95 (not shown). Mean profiles of relevant boundary-layer quantities are shown in Figure 9. The post-spin-up cloud field was roughly 200 m thick and gradually thinned to 160 m, with a peak liquid water content of 0.15 g/kg that varied minimally over the simulation period (Figure 9c). Mean boundary-layer TKE monotonically increased in time (Figure 8), despite decreasing cloud-top buoyancy integrals. Buoyancy flux integrals (negative area near cloud top in Figure 9d) in the 2–4 hr period were larger than 4–6 hr averages, but buoyant

TABLE 2 Decoupling parameter values for boundary-layer q_T and S_l

	$\psi(q_T)$	$\psi(S_l)$
CONTROL	0.039	0.014
	0.010	0.001
NOSUB	0.048	0.021
	0.029	0.012
0.25 cm/s	0.044	0.018
	0.018	0.008
0.5 cm/s	0.043	0.018
	0.014	0.005
0.75 cm/s	0.040	0.015
	0.011	0.003
1.25 cm/s	0.039	0.013
	0.012	0.002
1.5 cm/s	0.042	0.013
	0.039	0.032
LHF100	0.067	0.019
	0.021	0.009
LHF150	0.095	0.024
	0.084	0.031
SHF100	0.114	0.059
	–	–
NOSHEAR	0.042	0.015
	0.019	0.004
Directional	0.100	0.038
	–	–
PosVort	0.050	0.019
	0.074	0.045
NegVort	0.043	0.015
	0.013	0.001
ControlLW	0.017	0.006
	0.006	0.000
NOSUBLW	0.024	0.012
	0.010	0.004

Rows with simulation names correspond to 2–4 hr mean, while unlabeled rows correspond to 4–6 hr mean
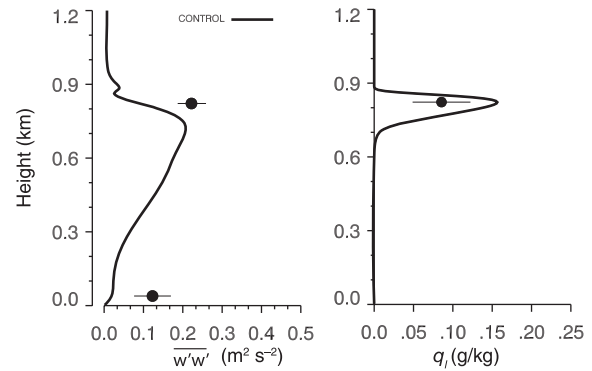

FIGURE 6 Aircraft observations from level legs (black dots). Vertical velocity variance and liquid water content in the cloud retrieved from 2105–2110 UTC. Vertical velocity variance near the surface averaged from 2120–2126 UTC. Model output averaged from 2045–2145 UTC. (a) Vertical velocity variance and (b) liquid water mixing ratio

3.2 | Sensitivity to variations in environmental forcing

In order to discover how thin stratocumulus responds to various forcing scenarios, the simulations explore changes in large-scale subsidence, wind shear across the inversion, surface fluxes, and radiative forcing. LES output from sensitivity tests was used to compare LES responses against known cloud/forcing relationships discussed in the literature, and to gain insights into how the modeled cloud evolves under wide ranges of environmental conditions using the mixed-layer budget approach that was outlined in section 2.4.

Sensitivity to changes in large-scale subsidence are of particular interest, because subsidence profiles are often poorly observationally constrained. Large-scale subsidence sensitivity was examined by applying a range of maximum subsidence values from 0–1.5 cm/s in the 900–6,000 m layer. The range of subsidence velocities indicated a nearly perfect negative linear correlation between subsidence rate and liquid water content in both the 2–4 and 4–6 hr averaging periods, with r^2 values greater than 0.95 (Figure 8). Mean boundary-layer TKE remains similar for cases where LWP exceeds 10 g/m^2 for the duration of the run (Figure 8), despite substantially different negative cloud-top buoyancy fluxes (Figure 10c). In general, decreasing subsidence scales linearly with mean boundary-layer depth, where a 1 cm/s increase in subsidence velocity results in an approximately 100 m shallower boundary layer over the course of the simulation. Although weaker subsidence runs result in deeper boundary layers and thus higher cloud tops (Figure 10e,f), the increased entrainment produces higher cloud-top temperatures and slightly increased long-wave cooling efficiency, owing to a decrease in air density (Stephens, 1978), which in turn causes greater long-wave radiative flux divergence. Additionally, thicker clouds and higher liquid water contents have a higher bulk infrared emissivity, approximated by the idealized functional dependence derived by Chylek and Ramaswamy (1982). Figure 10 shows increasing entrainment fluxes with weaker subsidence (−0.75–0 cm/s),
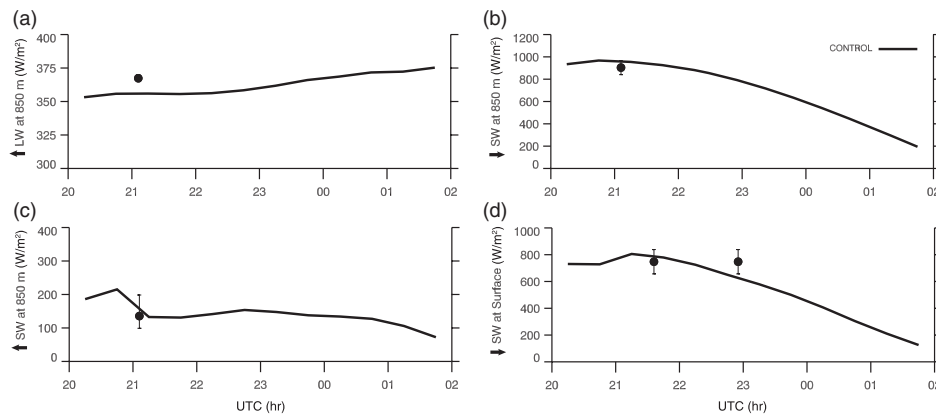
production of TKE was stunted by the initial stratification in the q_T profile. A small increase in vertical velocity variance was evident near the cloud top (Figure 9f), and through a TKE budget analysis this was found to be caused by weak shear-production of TKE (Appendix A). Inversion heights fell nearly 100 m over the course of the simulation as subsidence rates exceeded entrainment (Figure 9a). Cloud-top jump calculations indicate a gradual increase in stability of the inversion throughout the afternoon. The combination of low liquid water contents yet effective long-wave cooling led to a scenario where the cooling boundary layer allowed the cloud to remain relatively stable throughout the afternoon through limited entrainment and weak surface moisture fluxes. A simulation with no surface fluxes established that the small latent heat fluxes (4.45 W/m^2) play a very modest role in increasing LWP and cloud lifetime, only contributing to a difference of about 1 g/m^2.

FIGURE 7 Aircraft observations of radiative fluxes during level legs (black dots). Radiative fluxes averaged over duration of leg. (a) Upward long-wave radiative flux at 850 m, (b) downward short-wave radiative flux at 850 m, (c) upward short-wave radiative flux at 850 m, (d) downward short-wave radiative flux at the surface
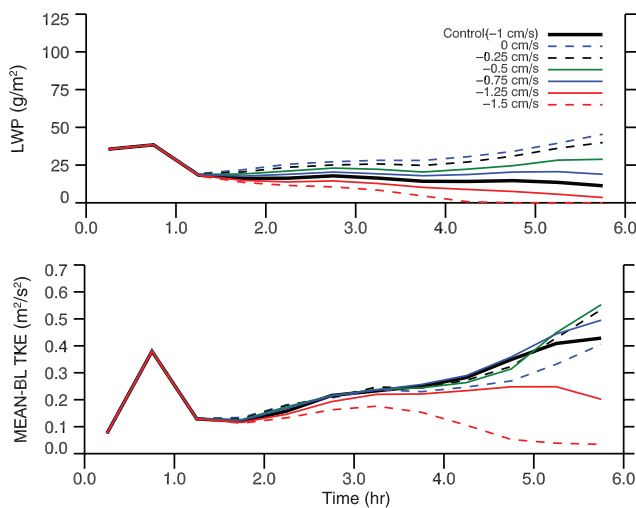

FIGURE 8 Liquid water path (LWP) and mean-BL TKE for a range of subsidence values from 0 to 1.5 cm/s. The solid black line is the control

likely stemming from the increasing long-wave radiative flux divergence. The decoupling is evident in weak subsidence cases (−0.25–0 cm/s) with peak vertical velocity values occurring in the cloud layer (Figure 10d) and subcloud negative buoyancy fluxes (Figure 10c), with the intrusion of warm, dry air into the cloud that is not able to be effectively mixed throughout the deeper boundary layer.

Analysis of a decoupling parameter (ψ) suggests that weaker subsidence produces stronger boundary-layer stratification that persists longer, in contrast to the control (Table 2), which is able to mix out most of the initial stratification. We suspect that the increased stratification ultimately limits the spread in mean-BL TKE trajectories. While stronger subsidence implies a stronger inversion through enhanced compressional warming, the reduced cloud water in the stronger subsidence cases plays an important role in inversion structure through a reduction in long-wave cooling at the cloud top. Sensitivity experiments involving only long-wave radiative fluxes demonstrated that efficient long-wave cooling maintains the inversion strength, but, in the presence of short-wave radiation, the reduction in LWP seen under

strong subsidence cases cannot maintain the sharp inversion structure (Figure 11).

Results from our suite of subsidence rate simulations are in agreement with recent studies performed by Myers and Norris (2013) and Van der Dussen *et al.* (2016). Myers and Norris (2013) determined observationally that, given a fixed value of inversion strength, decreasing subsidence would promote greater LWP. Since our weaker subsidence simulations were able to maintain inversion strength through stronger cloud-top cooling, the Myers and Norris (2013) assertion seems to hold true. Van der Dussen *et al.* (2016) found that solar absorption stunts the growth of the boundary layer initially, but eventually grows at a faster rate as entrainment rates increase later in the afternoon. Our simulations display a similar response, with the weaker subsidence runs having entrainment rates that typically increase monotonically with time.

Altering surface boundary conditions can emulate a variety of scenarios for stratocumulus clouds, including increased sensible heat fluxes (SHF) characteristic of the model domain passing over a warm land surface, or higher latent heat fluxes (LHF) associated with the warm side of the SST gradient. The surface fluxes were prescribed at a constant value for the duration of the simulations, and as a result no feedbacks that would naturally influence surface fluxes were represented. The fluxes were varied independently by specifying a sensible heat flux of 0 W/m² while latent heat fluxes were varied from 100–150 W/m², and vice versa. In sensitivity runs where sensible heat fluxes were large, the response was to increase mean-BL TKE greatly through surface buoyancy production. The increased surface buoyancy production leads to enhanced entrainment rates and cloud thinning. These findings are also corroborated by Ghonima *et al.* (2016), using LES and MLMs to determine stratocumulus lifetime given various surface forcings over land. Increasing LHF has been studied extensively in SCTs and found to be a primary mechanism for decoupling through enhancing entrainment fluxes, which dry the cloud layer disproportionately (Wyant *et al.*, 1997; Chung *et al.*, 2012; de Roode *et al.*, 2016). However, our simulations suggest the increased entrainment fluxes were compensated
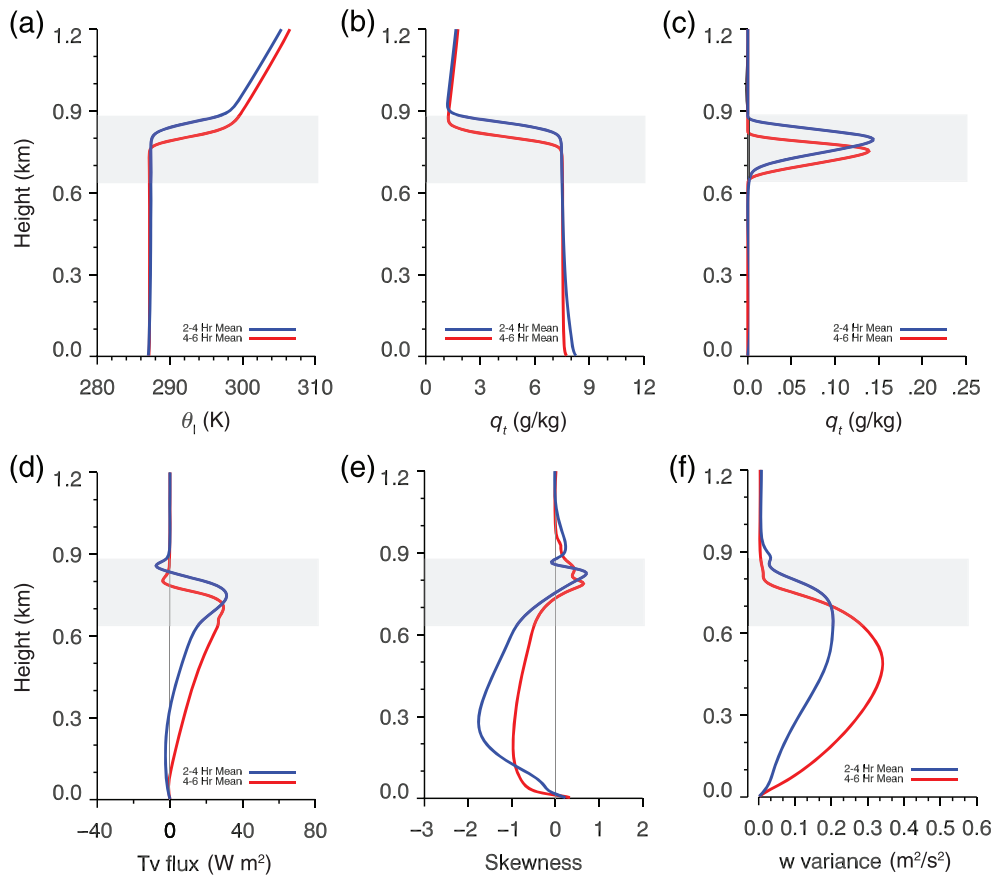
FIGURE 9 (a) Liquid potential temperature (θ_l), (b) total water mixing ratio (q_T), (c) liquid water mixing ratio (q_l), (d) buoyancy flux (T_v flux), (e) vertical velocity skewness, and (f) vertical velocity variance 2–4 and 4–6 hr mean profiles for the control run. The 2–4 hr cloudy region is shaded in gray
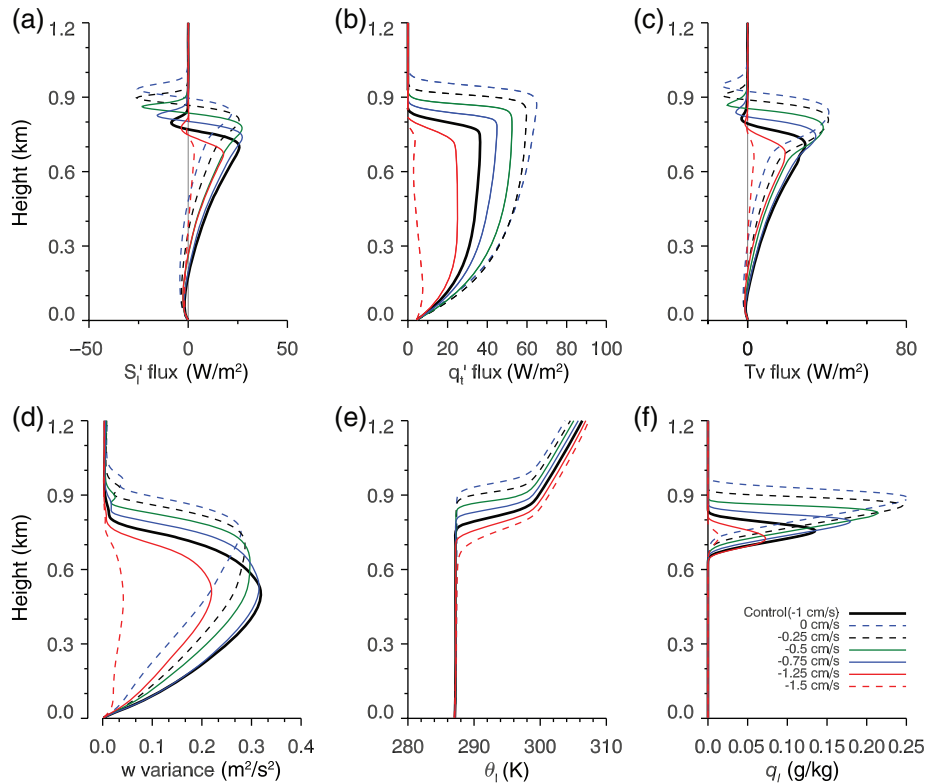

FIGURE 10 Sensitivity to subsidence rate (4–6 hr mean profiles): (a) S_l flux, (b) q_T flux, (c) buoyancy flux, (d) vertical velocity variance, (e) liquid potential temperature (θ_l), and (f) liquid water mixing ratio (q_l)
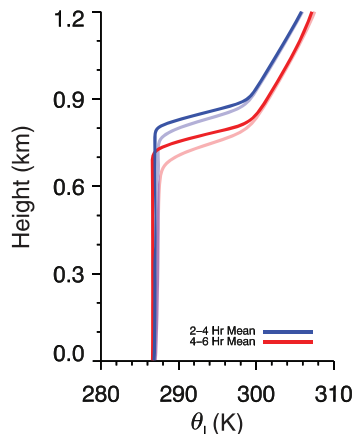
FIGURE 11 Dimmed lines: 1.5 cm/s subsidence with both short-wave and long-wave radiation present for duration of run Bold lines: 1.5 cm/s subsidence with only long-wave radiation present

by more efficient long-wave cooling and a constant moisture supply from below. Boundary-layer depth does not vary considerably, with deviations from the control being of the order of 10 m (Figure 12a), suggesting that the larger entrainment rates are still not sufficient to counteract subsidence. Regardless of substantial moisture stratification in the subcloud layer, the LHF simulations indicate no apparent decoupling in vertical velocity variance structure or buoyancy fluxes (Figure 12). The strong LHF case (150 W/m²) shows signs of cumulus coupling associated with the moisture stratification, which manifests itself as positive skewness in the subcloud layer (de Roode and Duynkerke, 1996).

Although much of the previous focus has been on the buoyancy production/consumption of TKE, wind shear near the inversion often has an important influence on cloud-top mixing and inversion structure, especially in our study region off the California coast, where a coastal jet is frequently observed (Wang *et al.*, 2008). Sensitivity to wind shear across the inversion was studied using four different scenarios.

1. No shear, with flow invariable with height out of the northwest at 6.4 m/s (NO SHEAR).
2. Directional shear with southeasterly winds in the boundary layer (0–900 m) and northwesterly winds above 925 m,

with both having a velocity magnitude of 6.4 m/s (DIRECTIONAL).
3. Speed shear that induced positive vorticity near the inversion, with a velocity magnitude of 6.4 m/s from 0–900 m and 12.8 m/s from 925–1500 m, thereafter it relaxed back to 6.4 m/s (SPEED +vort).
4. Speed shear that induced negative vorticity near the inversion, with a velocity magnitude of 12.8 m/s from 0–900 m and 6.4 m/s from 925 m and above (SPEED −vort).

Increased wind shear resulted in lower liquid water content and reduced mean-BL TKE through the enhancement of cloud-top mixing. As the cloud water is diminished, the production of negative cloud-top buoyancy is limited and entrainment rates are reduced. Inversion heights were found to decrease as wind shear was increased, which Wang *et al.* (2008) determined would occur under weaker and more diffuse inversions. Initially, cloud-top mixing is increased through enhanced shear production of TKE, but an attendant decrease in entrainment rate occurs as liquid water content is reduced considerably. Figure 13 shows the evolution of inversion depth and inversion base height, as well as the existence of a deep cloud-free turbulent sublayer within the inversion, which has been observed and modeled in previous studies exploring the gap between cloud-top and turbulent mixing interfaces (Lenschow *et al.*, 2000; Moeng *et al.*, 2005). Speed shear simulations associated with equal magnitudes of positive and negative horizontal vorticity are not equivalent, with positive speed shear (Figure 13, solid blue) initially producing greater TKE near the cloud top through the relaxation of the winds above 1,500 m, but, as liquid water contents decrease from greater mechanical mixing, the buoyant production of TKE is significantly reduced. The negative horizontal vorticity run (Figure 13, dashed blue) exhibits little deviation from the control, with no evident change in inversion-layer depth despite slightly larger TKE near 900 m in the 4–6 hr period. Overall, our LES results corroborate previous findings on the effects of wind shear on turbulent production and cloud evolution.

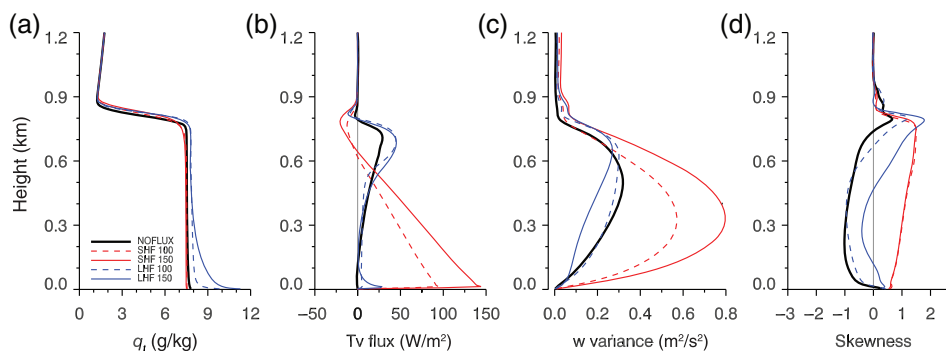Radiative forcing sensitivity was investigated by examining LES output under two different scenarios in the

FIGURE 12 4–6 hr mean profiles of (a) total water mixing ratio q_T, (b) buoyancy flux ($T_v flux$), (c) vertical velocity variance (w variance), and (d) skewness for SHF/LHF ranging from 100–150 W/m²
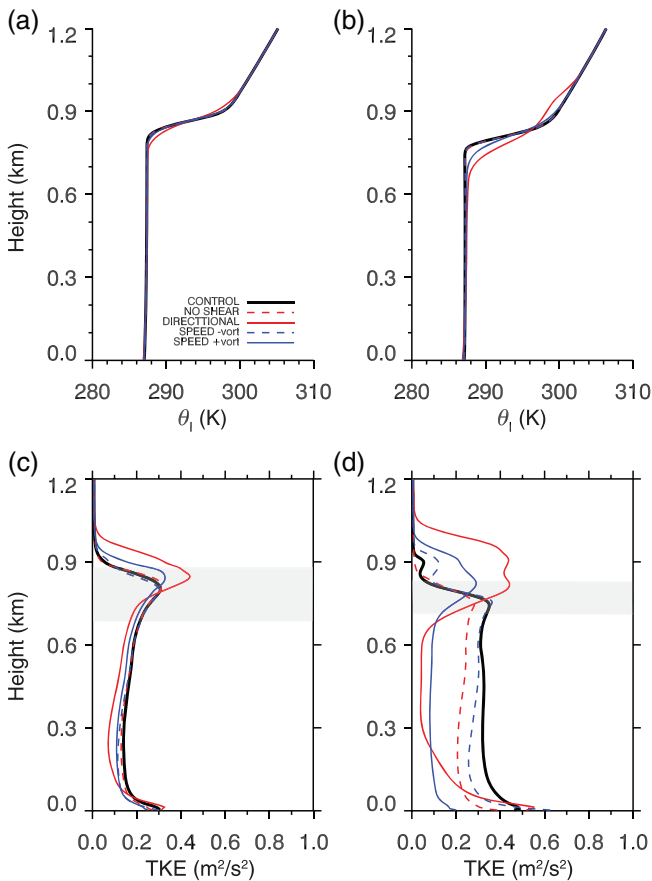
FIGURE 13 (a,c) 2–4 hr mean profile of (a) θ_l and (c) TKE. (b,d) 4–6 hr mean profile of (b) θ_l and (d) TKE. The gray shaded region represents the mean cloud layer of the directional shear run (DIRECTIONAL)

FIGURE 14 Liquid water mixing ratio (q_l) profiles for 2–4 and 4–6 hr means

absence of short-wave radiation (Control and NOSUB), in an attempt to isolate the implications of short-wave absorption. Nocturnal stratocumulus has been studied extensively observationally and through various modeling approaches, given the near-equilibrium/steady-state behavior. Stronger convective circulations are observed at night, as long-wave cooling drives negative buoyancy production and the boundary layer remains well-mixed. This efficient coupling with the surface moisture supply for cases of larger surface evaporation/LHF is crucial for sustaining the cloud (Turton and Nicholls, 1987), but, in our control case, moisture flux from the ocean surface is so small that the initial increase in entrainment is not compensated by an increased water-vapor flux (fixed latent heat flux in LES) from the surface and cloud thickness decreases with time, as shown in Figure 14. The rate at which the control long-wave-only simulation is entraining free-tropospheric air into the boundary layer is less than the subsidence rate, given the falling cloud-top heights (Figure 14). The NOSUB long-wave-only simulation indicates a thickening of the cloud with time and higher peak liquid water contents (Figure 14).

Using a method similar to studies attempting to quantify the susceptibility of cloud albedo (Platnick and Twomey, 1994) and precipitation (Sorooshian *et al.*, 2009) to changes in droplet concentration, the sensitivity of LWP to changes in
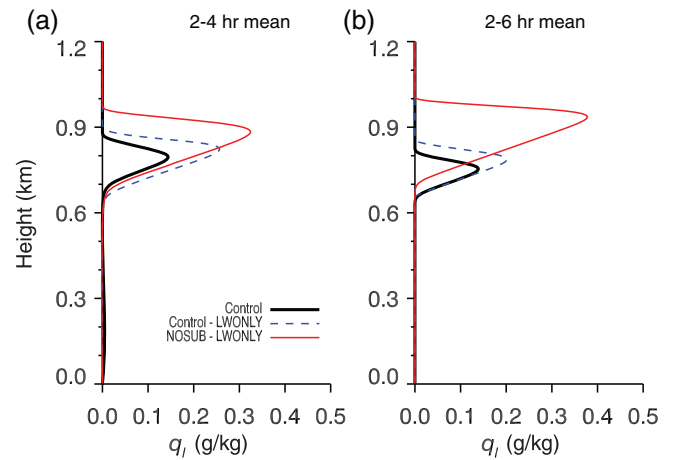
different environmental forcings can be calculated. In particular, we are interested in the relative importance of the various forcings, such as large-scale vertical motion, and latent and sensible heat fluxes. In other words, to which of these forcing terms is the simulated LWP most sensitive? The susceptibility parameter (S_0) is calculated according to Equation 10, where p represents the environmental forcing parameter and $\overline{p}$ and $\overline{LWP}$ are the respective mean values. The analysis was performed at 2.75 hr, near the simulation midpoint, where all runs had a LWP greater than zero. LWP susceptibility to a changing subsidence rate is substantial ($S_0 = 0.41$), while the LWP is less susceptible to changes in latent heat flux ($S_0 = 0.14$). LWP appears most susceptible to changes in sensible heat flux ($S_0 = 1.01$), but the large values of sensible heat flux in our simulations are much larger than typically seen over coastal regions in the subtropics and midlatitudes, so the sensible heat flux value probably has little practical value.

$$S_0 \frac{\overline{LWP}}{\overline{p}} = \frac{d(LWP)}{dp} \qquad (10)$$

3.3 | Control mixed-layer budget analysis

Figure 15 shows the individual budget terms contributing to changes in the MLM cloud-base tendency Equation 7, along with the net cloud-base tendency diagnosed by the MLM (the sum of the terms on the right-hand side of Equation 7, denoted as 'Net' in Figure 15) and the cloud-base tendency derived from LES results. Changes in cloud-base height are governed by the entrainment warming/drying and short-wave absorption, which act to raise the cloud base, and long-wave cooling, which acts to lower the saturation point and thicken the cloud. The stronger stratification in the first analysis period leads to fairly large discrepancies between the MLM and the LES. The magnitudes of cloud-base tendency errors associated with q_T and S_l budgets can be approximated by inputting model budget tendencies into Equation 7. Budget errors are responsible for an overestimation of entrainment
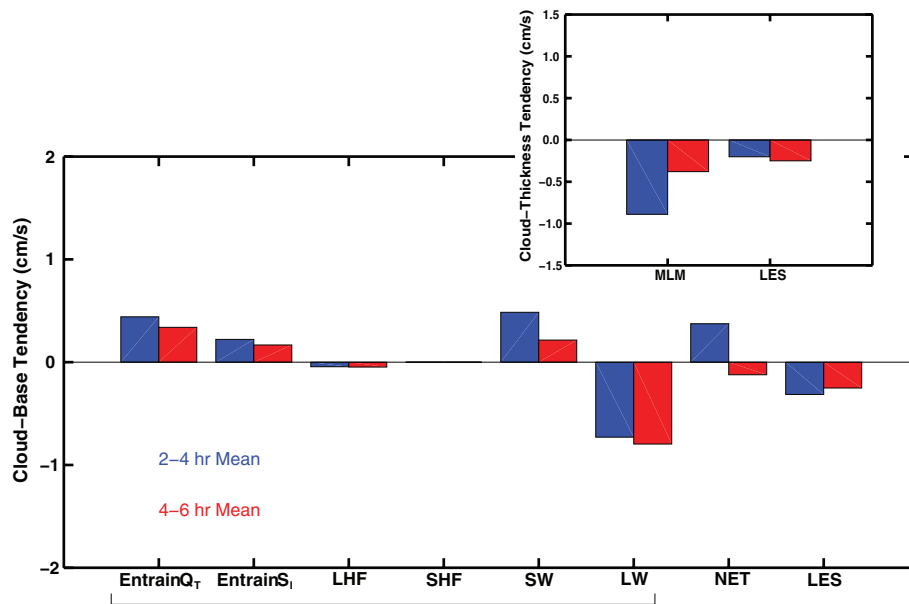
FIGURE 15 Individual budget terms from left to right: q_T entrainment flux (EntrainQ_T), S_l entrainment flux (EntrainS_l), latent heat flux (LHF), sensible heat flux (SHF), short-wave radiative flux divergence (SW), and long-wave radiative flux divergence (LW). The sum of bracketed terms is the 'NET' of budget terms and LES refers to the cloud-base tendency diagnosed from the LES. Negative values indicate a lowering of the cloud base. Top right panel: cloud-thickness tendency (negative values indicate thinning cloud)

drying of approximately 0.13 cm/s and an underestimation of drying of about −0.05 cm/s in the 2–4 and 4–6 hr periods, respectively. The remainder of the errors are attributed to decoupling (not evenly distributed over boundary-layer depth) in the LES and the accuracy of the model-derived cloud-base, which is limited by vertical grid spacing. As the boundary-layer becomes well-mixed, the MLM cloud-base tendencies are more aligned with the LES. Even in the presence of substantial short-wave heating, the entrainment fluxes remain active. Entrainment fluxes in both analysis periods are likely comparable in size, but definitive conclusions about the evolution of the magnitude of the entrainment fluxes cannot be drawn in this particular case, because of uncertainties regarding boundary-layer stratification. However, the budget terms indicate that cloud-base height increases caused by the entrainment of dry air are likely larger than those associated with the entrainment of warmer (higher S_l) free tropospheric air. The small amount of surface moisture flux (LHF) remains constant in time and plays a minor role in reducing cloud-base heights, as the temperature of the cloud base and the depth of the boundary layer do not change the small fixed value drastically. Short-wave warming contributes to cloud-base rises and decreases substantially from the first to second analysis period, as expected with decreasing insolation as the afternoon progresses. The only source of direct boundary-layer cooling in our case is through positive long-wave flux divergence, which remains fairly constant in time, increasing slightly in the 4–6 hr period because of the shallower boundary layer. In this thin cloud case, the long-wave cooling was able to overcome the drying and warming terms to result in a net cooling and lowering of the cloud-base. Figure 15 also shows

the cloud-thickness tendency throughout the afternoon, with cloud thickness decreasing despite falling cloud bases, as the inversion base is decreasing faster than the cloud base is lowering.

3.4 | Mixed-layer budget analysis for sensitivity simulations

As subsidence weakens from −1.5 to 0 cm/s, the cloud-base rises associated with the entrainment fluxes increase, with the q_T entrainment flux once again contributing to greater cloud-base rises than entrainment fluxes (Table 3). Relative to the control run, the short-wave radiative flux divergence contribution to cloud-base tendency did not vary over 0.05 cm/s in all cases, indicating an insensitivity stemming from the increase in boundary-layer depth. The relative importance of the long-wave radiative flux divergence also remains steady, increasing with weakening subsidence by no more than 0.15 cm/s. While net radiative flux divergence remains nearly constant between varying subsidence cases, the weaker subsidence runs are not able to counteract the enhanced entrainment fluxes, resulting in boundary-layer warming and drying and a rise in cloud base. As the afternoon progresses, the reduction in short-wave flux divergence is often enough to nearly overcome the enhanced entrainment, and a reduction in either cloud-base rises or cloud-base falls ensue. The MLM S_l budget tendency in the 2–4 hr period underestimates the warming (Table 1), which is more than likely attributable to an underestimation of the S_l entrainment fluxes. As discussed in section 2.5, under weaker subsidence the boundary-layer was not able to reach a well-mixed state by the end of the second period and remained slightly decoupled, which we

TABLE 3 Contribution of individual budget terms to cloud-base tendency

	EntrainQT	EntrainSL	LHF	SHF	SW	LW	Net	Model
				(cm/s)				
CONTROL	0.44	0.22	−0.044	0.00	0.48	−0.73	0.37	−0.31
	0.34	0.17	−0.047	0.00	0.21	−0.80	−0.12	−0.25
NOSUB	0.57	0.36	−0.041	0.00	0.52	−0.81	0.61	0.22
	0.53	0.35	−0.040	0.00	0.22	−0.82	0.23	−0.18
0.25 (cm/s)	0.54	0.33	−0.042	0.00	0.51	−0.79	0.55	0.09
	0.51	0.31	−0.042	0.00	0.22	−0.85	0.14	−0.23
0.5 (cm/s)	0.51	0.30	−0.042	0.00	0.50	−0.77	0.49	−0.03
	0.46	0.27	−0.044	0.00	0.21	−0.86	0.04	−0.27
0.75 (cm/s)	0.49	0.27	−0.043	0.00	0.49	−0.77	0.44	−0.20
	0.41	0.22	−0.045	0.00	0.21	−0.86	−0.07	−0.22
1.25 (cm/s)	0.39	0.17	−0.045	0.00	0.48	−0.68	0.32	−0.39
	0.20	0.09	−0.050	0.00	0.23	−0.61	−0.13	−0.23
1.5 (cm/s)	0.29	0.12	−0.046	0.00	0.47	−0.56	0.27	−0.30
	0.04	0.02	−0.050	0.00	0.35	−0.23	0.12	−0.06
*LHF*100	0.62	0.34	−0.970	0.00	0.50	−0.71	−0.21	−0.76
	0.76	0.39	−1.000	0.00	0.23	−0.81	−0.43	−0.53
*LHF*150	0.58	0.33	−1.440	0.00	0.52	−0.76	−0.77	−2.30
	0.92	0.54	−1.480	0.00	0.24	−0.84	−0.62	0.77
*SHF*100	0.60	0.36	0.000	1.28	0.54	−0.89	1.86	1.44
	–	–	–	–	–	–	–	–
NOSHEAR	0.44	0.23	−0.044	0.00	0.48	−0.70	0.43	−0.24
	0.30	0.19	−0.048	0.00	0.22	−0.70	−0.03	−0.34
Directional	0.40	0.32	−0.046	0.00	0.47	−0.48	0.65	−0.50
	–	–	–	–	–	–	–	–
PosVort	0.43	0.26	−0.045	0.00	0.47	−0.63	0.48	−0.16
	0.15	0.12	−0.048	0.00	0.31	−0.36	0.17	0.09
NegVort	0.40	0.20	−0.044	0.00	0.48	−0.71	0.34	−0.41
	0.35	0.19	−0.048	0.00	0.22	−0.75	−0.04	−0.24
ControlLW	0.71	0.39	−0.044	0.00	0.00	−0.74	0.32	−0.10
	0.46	0.25	−0.047	0.00	0.00	−0.77	−0.12	−0.05
NOSUBLW	0.78	0.54	−0.040	0.00	0.00	−0.80	0.48	0.24
	0.60	0.44	−0.040	0.00	0.00	−0.78	0.22	0.31

Positive (negative) values indicate a rising (falling) cloud base. Net is the sum of the individual budget terms and model is the LES cloud-base tendency. Rows with simulation names correspond to the 2–4 hr mean, while unlabeled rows correspond to the 4–6 hr mean

speculate is responsible for most of the deviations from the LES (Table 3).

Surface flux sensitivity tests resulted in the largest budget q_T uncertainties of all the simulations, with 100% of the available analysis periods (five 2-hr periods) suffering from relative errors greater than 0.50 (Table 1). There were also several significant errors in the MLM S_l budget tendencies, associated with overestimation of warming in the 2–4 hr period. For the strong LHF run (150 W/m), the model budgets reveal an expected positive q_T tendency and a small negative S_l tendency. Model cloud-base tendency also indicates a reversal of cloud-base tendency, with 2–4 hr mean cloud-base falls and 4–6 hr mean cloud-base rises. Although the MLM struggles with the exact magnitude of entrainment mixing for both q_T and S_l for the surface flux sensitivity runs, it seems to capture the general increase in entrainment fluxes that model

tendencies suggest. With budget errors imposing uncertainty in cloud-base tendency budget terms and the largest values of decoupling of any of the simulations, a meaningful cloud-base tendency budget analysis of the surface flux sensitivity suite is difficult.

The sensitivity tests with no shear evolved quite similarly to the control, but the lack of mechanical mixing near the cloud top did not mix the entrainment fluxes sufficiently in the layer from the inversion base to the S_l flux minimum, and the actual entrainment flux experienced by the boundary layer was of a smaller magnitude and closer to the inversion base. The opposite is true for the directional wind shear case, where increased shear production of TKE significantly weakened and deepened the inversion layer. The entrainment flux estimation method underestimates the depth of the entrainment layer in the directional shear case,

leading to an overestimation of entrainment flux strength in the MLM. Much like the surface flux sensitivity tests, the budget uncertainties are thought to stem primarily from the method of entrainment calculation, which fails to incorporate physical processes that may alter the entrainment-layer depth. The magnitude of entrainment fluxes in both analysis periods for all shear sensitivity cases remained similar to the control, owing to the directional and positive vorticity runs depleting liquid water content enough before the 2-hr mark that entrainment fluxes began to decrease. The sensitivity run that induced positive horizontal vorticity near the cloud top warmed the boundary layer during the 2–4 hr period, while the negative horizontal vorticity run cooled. This contrast can be explained by the increased long-wave cooling in the negative horizontal vorticity case, which had a slightly higher liquid water content.

The long-wave-only simulations based on the control and no-subsidence set-ups underestimated entrainment warming and drying in all averaging periods. The control long-wave-only simulation had small relative errors, while the no-subsidence long-wave-only run underestimated the warming contribution of S_l substantially (relative errors 0.91 and 0.56, see Table 1). Boundary-layer drying is greatest during the 2–4 hr period, while boundary-layer cooling is greatest in the 4–6 hr period in both long-wave-only cases. The q_T entrainment fluxes are approximately 60–80% larger and S_l entrainment fluxes are 70–145% larger than the control (Table 3). Entrainment fluxes decrease appreciably from the first to the second analysis period. This may be partly associated with weak stratification early in the period (isolated updraft activity) or, more likely, ascribed to increased inversion strength. Model cloud-base tendencies are very close to zero in the control long-wave-only simulation, and with negative inversion tendencies, resulting in cloud thinning. The no-subsidence long-wave-only run entrains slightly more than the control long-wave-only run, but the growing boundary layer produces positive cloud-thickness tendencies (Table 3).

4 | SUMMARY AND CONCLUSIONS

This study aimed to determine the dominant mechanisms governing the evolution of thin afternoon marine stratocumulus through the application of mixed-layer theory to LES output. Aircraft observations obtained during the first research flight of the UPPEF field campaign were used to constrain and validate model behavior. The evaluation of individual physical mechanisms modulating cloud properties in a highly nonlinear, turbulent boundary-layer flow is nearly intractable when analyzing LES output alone. We instead analyze the LES output in the framework of a mixed-layer model budget. In an effort to reduce complexity, budgets of q_T and S_l were partitioned into moisture and energy source/sink terms, as put forth by Caldwell et al. (2005). The budgets were extended further to incorporate the relationship between cloud-base

tendency and changes in q_T and S_l budgets (Wood, 2007; Ghonima et al., 2015). In doing so, attributing relative contributions of each source/sink term to boundary-layer moisture can be deduced. The thin cloud response to a wide range of environmental forcing scenarios was examined by running a multitude of sensitivity tests.

As shown here, the mixed-layer cloud-base tendency approach can be a useful tool to discern which terms are most responsible for changes in boundary-layer saturation, which may not be possible by examining LES output independently. Our main findings are summarized in the following points.

- Despite substantial solar fluxes during the afternoon, which are typically understood to suppress TKE production and reduce entrainment relative to a nocturnal cloud-topped boundary layer, entrainment fluxes that warm and dry the cloud layer remain strongly active.
- In terms of cloud-base tendency, the magnitude of the reduction in solar warming later in the afternoon in most of our simulations is larger than the changes in entrainment fluxes from early afternoon to later in the evening (either increases or decreases), causing a relative lowering of the cloud base with respect to early afternoon and a recovery of the cloud. However, in the case of the control, the reduced entrainment fluxes led to a faster lowering of the inversion base and thinned the cloud.
- In the absence of significant surface or advective forcing, entrainment fluxes are the main mechanisms governing the overall sign of the cloud base. All simulations suggest that the q_T entrainment flux contributes more toward the evolution of cloud-base height than the S_l flux. The dependence on entrainment fluxes arises from the insensitivity of the net radiative flux divergence term for simulations with LWP in the 10–50 g/m^2 range (Table 3).
- Sensitivity experiments varying subsidence, surface fluxes, shear, and radiative forcing produced largely predictable outcomes, including confirmation of previous studies that investigated the relationship between LWP and subsidence.

While the MLM approach is a viable method to attain our research goals, this particular case presents several challenges. The inversion associated with the thin cloud is rather diffuse, violating the zero-order cloud-top jump assumption traditionally assumed in mixed-layer theory. The standard flux-jump formulation for the entrainment flux closure typically used in MLMs is not appropriate for our more diffuse inversion structure and requires a different approach. We found the most robust method to be a layer average of explicitly resolved LES entrainment fluxes from the inversion base to the height of the minimum S_l flux. Error analysis of LES and MLM budgets suggests that the method does not capture all of the physical processes that contribute to varying depths of the entrainment layer, with systematic biases overestimating warming and drying during the 2–4 hr period and underestimating them during the

4–6 hr period. Future work should emphasize uncertainties regarding entrainment-layer depth and perhaps relate to more physically based variables such as cloud-top gradients, net radiative flux divergence, liquid water content, and specific TKE characteristics near the cloud top. The entrainment flux calculations introduce the main source of uncertainties in the q_T and S_l budgets, but often do not translate to significant errors in cloud-base tendency, with the exception of surface flux and shear sensitivity runs. Additional research is also necessary for the possibility of separate entrainment-layer depths for q_T and S_l. The main source of uncertainty in cloud-base tendency budgets can be accredited to boundary-layer stratification. However, by utilizing the conserved LES budget tendencies, as opposed to the cloud-base tendency alone (a residual quantity), the error contribution from stratification can be estimated and factored into the analysis, since the errors lead to a consistent overestimation of positive cloud-base tendencies (cloud-base rises).

The control simulation agreed reasonably well with the available observations of vertical velocity variance, liquid water content, and radiative fluxes. Over the course of the afternoon, the control run underwent gradual cloud thinning in terms of both cloud thickness and LWP. The development of boundary-layer-depth eddies during the latter half of the simulation effectively distributed subcloud moisture into the cloud layer, and the boundary layer was able to become well-mixed. Mixed-layer budget analysis suggests that the entrainment flux contributions to cloud-base rises are near comparable in magnitude in both analysis periods, despite increased long-wave cooling in the 4–6 hr period. We hypothesize that this may be a result of isolated cumulus development in the 2–4 hr period associated with initial moisture stratification and increasing stability later in the afternoon. In this weak surface moisture flux case, the only way to lower the cloud base is through changing the saturation point via long-wave cooling. The thin cloud long-wave cooling is large enough to overcome short-wave warming and entrainment of warm/dry free tropospheric air (especially evident in the 4–6 hr period), which results in a lowering of the cloud base, but the lowering inversion tendency remains larger than the cloud-base lowering, leading to gradual cloud thinning.

Liquid water content was found to increase linearly with a decrease of subsidence velocity, and mean-BL TKE values were found to remain quite similar, with weaker subsidence promoting increased stratification through disproportionately warming and drying the cloud layer with increased entrainment rates. The increased warm-air entrainment, latent heating, and solar absorption all act to warm cloud-top temperatures (despite higher cloud tops), which increases long-wave radiative flux divergence slightly for weaker subsidence. Also, the increased liquid water content in weaker subsidence cases results in a higher infrared emissivity (stronger long-wave cooling: Chylek and Ramaswamy, 1982), which,

combined with the warmer cloud-top temperatures, promotes larger cloud-top entrainment fluxes. Mixed-layer budget analysis indicates that the increase in depth of the boundary layer in weaker subsidence simulations negates the increased net radiative flux divergence, resulting in an insensitivity between subsidence rate and radiative cooling effects on cloud-base tendency. The weaker subsidence runs entrain more and therefore they dry and warm during the early afternoon, but, as time progresses and short-wave warming subsides, this transitions to cooling. Simulations with no short-wave radiation resulted in entrainment fluxes that were much larger than the control and decreased in time in response to a strengthening inversion. A detailed cloud-base tendency budget analysis of runs changing the degree of wind shear near the inversion and surface-flux sensitivity tests was not presented, due to larger budget uncertainties in comparison with the model and higher degrees of stratification. In an effort to determine the sensitivity of LWP to various environmental forcing scenarios, a susceptibility analysis was performed. LWP was found to be quite sensitive to subsidence velocity and relatively insensitive to LHF.

The research presented here remains loosely observationally constrained, with a lack of level legs in or near the cloud top and few full soundings to gather meaningful LWP estimates from aircraft. This particular case presented many challenges, both in terms of modeling a thin, afternoon stratocumulus deck reasonably and representing LES fields in a mixed-layer framework. Future work may focus on ways of diagnosing entrainment-layer depth based on physical quantities, such as liquid water content, subsidence rate, inversion strength, and so on. Regardless of the challenges presented in this case, attribution of cloud-governing mechanisms to cloud evolution was possible through an in-depth analysis of LES and MLM budget comparisons.

ACKNOWLEDGEMENTS

ORCID

Lucas A. McMichael https://orcid.org/0000-0003-0980-370X

REFERENCES

Ackerman, A., Kirkpatrick, M.P., Stevens, D.E. and Toon, O.B. (2004) The impact of humidity above stratiform clouds on indirect aerosol climate forcing. *Nature*, 432, 1014–1017.

Albrecht, B.A., Randall, D.A. and Nicholls, S. (1988) Observations of marine stratocumulus clouds during fire. *Bulletin of the American Meteorological Society*, 69, 618–626.

Bretherton, C.S. and Wyant, M.C. (1997) Moisture transport, lower-tropospheric stability, and decoupling of cloud-topped boundary layers. *Journal of the Atmospheric Sciences*, 54, 148–167.

Bretherton, C.S., Blossey, P.N. and Uchida, J. (2007) Cloud droplet sedimentation, entrainment efficiency, and subtropical stratocumulus albedo. *Geophysical Research Letters*, 34, L03813. https://doi.org/10.1029/2006GL027648.

Burleyson, C.D. and Yuter, S. (2015) Patterns of diurnal marine stratocumulus cloud fraction variability. *Journal of Applied Meteorology and Climatology*, 54, 847–866.

Burleyson, C.D., Szoeke, S.P.D., Yuter, S.E., Wilbanks, M. and Brewer, W.A. (2013) Ship-based observations of the diurnal cycle of southeast pacific marine stratocumulus clouds and precipitation. *Journal of the Atmospheric Sciences*, 70, 3876–3894.

Caldwell, P. and Bretherton, C.S. (2009) Large eddy simulation of the diurnal cycle in Southeast Pacific stratocumulus. *Journal of the Atmospheric Sciences*, 66, 432–449.

Caldwell, P., Wood, R. and Bretherton, C.S. (2005) Mixed-layer budget analysis of the diurnal cycle of entrainment in Southeast Pacific stratocumulus. *Journal of the Atmospheric Sciences*, 62, 3775–3791.

Chen, T., Rossow, W.B. and Zhang, Y.C. (2000) Radiative effects of cloud-type variations. *Journal of Climate*, 13, 264–286.

Chung, D., Matheou, G. and Teixeira, J. (2012) Steady-state large-eddy simulations to study the stratocumulus to shallow cumulus cloud transition. *Journal of the Atmospheric Sciences*, 69, 3264–3276.

Chylek, P. and Ramaswamy, V. (1982) Simple approximation for infrared emissivity of water clouds. *Journal of the Atmospheric Sciences*, 39, 171–177.

Collins, W.D., Bitz, C.M., Blackmon, M.L., Bonan, G.B., Bretherton, C.S., Carton, J.A., Chang, P., Doney, S.C., Hack, J.J., Henderson, T.B., Kiehl, J.T., Large, W.G., McKenna, D.S., Santer, B.D. and Smith, R.D. (2006) The Community Climate System Model version 3 (CCSM3). *Journal of Climate*, 19, 2122–2143.

Comstock, K., Wood, R., Yuter, S. and Bretherton, C.S. (2004) Radar observations of precipitation in and below stratocumulus clouds. *Quarterly Journal of the Royal Meteorological Society*, 130, 2891–2918.

Deardoff, J. (1980) Stratocumulus-capped mixed layers derived from a three-dimensional model. *Boundary-Layer Meteorology*, 18, 495–527.

Feingold, G., Stevens, B., Cotton, W.R. and Frisch, A.S. (1996) The relationship between drop in-cloud residence time and drizzle production in numerically simulated stratocumulus clouds. *Journal of the Atmospheric Sciences*, 53, 1108–1122.

Ghonima, M.S., Norris, J.R., Heus, T. and Kleissl, J. (2015) Reconciling and validating the cloud thickness and liquid water path tendencies proposed by R. Wood and JJ van der Dussen et al. *Journal of the Atmospheric Sciences*, 72, 2033–2040.

Ghonima, M.S., Heus, T., Norris, J.R. and Kleissl, J. (2016) Factors controlling stratocumulus cloud lifetime over coastal land. *Journal of the Atmospheric Sciences*, 73, 2961–2983.

Hartmann, D.L. and Short, D. (1980) On the use of earth radiation budget statistics for studies of clouds and climate. *Journal of the Atmospheric Sciences*, 37, 1233–1250.

Hodur, R.M. (1997) The Naval Research Laboratory's Coupled Ocean/Atmosphere Mesoscale Prediction System (COAMPS). *Monthly Weather Review*, 125, 1414–1430.

Jiang, H., Feingold, G. and Cotton, W.R. (2002) Simulations of aerosol-cloud-dynamical feedbacks resulting from entrainment of aerosol into the marine boundary layer during the Atlantic Stratocumulus Transition Experiment.

Journal of Geophysical Research, 107, AAC 20-1–20-9. https://doi.org/10.1029/2001JD001502.

Kessler, E. (1969) *On the Distribution and Continuity of Water Substance in Atmospheric Circulations*. Meteorological Monographs 32. Boston, MA: American Meteorological Society.

Khairoutdinov, M.F. and Randall, D.A. (2003) Cloud resolving modeling of the ARM summer 1997 IOP: model formulation, results, uncertainties, and sensitivities. *Journal of the Atmospheric Sciences*, 60, 607–625.

Klein, S.A. and Hartmann, D.L. (1993) The seasonal cycle of low stratiform clouds. *Journal of Climate*, 6, 1588–1606.

Lenschow, D.H., Zhou, M., Zeng, Z., Chen, L. and Xu, X. (2000) Measurements of fine-scale structure at the top of marine stratocumulus. *Boundary-Layer Meteorology*, 97, 331–357.

Leon, D.C., Wang, Z. and Liu, D. (2008) Climatology of drizzle in marine boundary layer clouds based on 1 year of data from Cloudsat and Cloud-Aerosol Lidar and Infrared Pathfinder Satellite Observations (CALIPSO). *Journal of Geophysical Research*, 113, D00A14. https://doi.org/10.1029/2008JD009835.

Lewellen, D.C. and Lewellen, W.S. (1998) Large-eddy boundary layer entrainment. *Journal of the Atmospheric Sciences*, 55, 2645–2665.

Moeng, C.-H., Stevens, B. and Sullivan, P.P. (2005) Where is the interface of stratocumulus-topped PBL? *Journal of the Atmospheric Sciences*, 62, 2626–2631.

Monin, A.S. and Obukhov, A.M. (1954) Basic laws of turbulent mixing in the atmosphere near the ground. *Trudy Akademiya Nauk SSSR Geofizicheskogo Instituta*, 24, 163–187.

Myers, T.A. and Norris, J. (2013) Observational evidence that enhanced subsidence reduces subtropical marine boundary layer cloudiness. *Journal of Climate*, 26, 7505–7524.

Nicholls, S. (1984) The dynamics of stratocumulus: aircraft observations and comparisons with a mixed layer model. *Quarterly Journal of the Royal Meteorological Society*, 110, 783–820.

Nicholls, S. and Leighton, J. (1986) An observational study of the structure of stratiform cloud sheets: Part I. Structure. *Quarterly Journal of the Royal Meteorological Society*, 112, 431–460.

Park, S., Leovy, C.B. and Rozendaal, M.A. (2004) A new heuristic Lagrangian marine boundary layer cloud model. *Journal of the Atmospheric Sciences*, 61, 3002–3024.

Platnick, S. and Twomey, S. (1994) Determining the susceptibility of cloud albedo to changes in droplet concentration with the Advanced Very High Resolution Radiometer. *Journal of Applied Meteorology*, 33, 334–347.

Randall, D.A. (1980) Conditional instability of the first kind upside down. *Journal of the Atmospheric Sciences*, 37, 125–130.

de Roode, S.R. and Duynkerke, P.G. (1996) Dynamics of cumulus rising into stratocumulus as observed during the first 'Lagrangian' experiment of ASTEX. *Quarterly Journal of the Royal Meteorological Society*, 122, 1597–1623.

de Roode, S.R., Sandu, I., Van Der Dussen, J.J., Ackerman, A.S., Blossey, P., Jarecka, D., Lock, A., Siebesma, A.P. and Stevens, B. (2016) Large-eddy simulations of EUCLIPSE–GASS Lagrangian stratocumulus-to-cumulus transitions: mean state, turbulence, and decoupling. *Journal of the Atmospheric Sciences*, 73, 2485–2508.

Rozendaal, M.A., Leovy, C.B. and Klein, S.A. (1995) An observational study of the diurnal cycle of marine stratiform cloud. *Journal of Climate*, 8, 1795–1809.

Sandu, I. and Stevens, B. (2011) On the factors modulating the stratocumulus to cumulus transitions. *Journal of the Atmospheric Sciences*, 68, 1865–1881.

Sandu, I., Brenguier, J.L., Geoffroy, O., Thouron, O. and Masson, V. (2008) Aerosol impacts on the diurnal cycle of marine stratocumulus. *Journal of the Atmospheric Sciences*, 65, 2705–2718.

Sears-Collins, A.L., Schultz, D.M. and Johns, R.H. (2006) Spatial and temporal variability of nonfreezing drizzle in the United States and Canada. *Journal of Climate*, 19, 3629–3639. Corrigendum, 21, 1447–1448.

Sorooshian, A., Feingold, G., Lebsock, M.D., Jiang, H. and Stephens, G.L. (2009) On the precipitation susceptibility of clouds to aerosol perturbations. *Geophysical Research Letters*, 36, L13803. https://doi.org/10.1029/2009GL038993.

Stephens, G.L. (1978) Radiation profiles in extended water clouds: 1. Theory. *Journal of the Atmospheric Sciences*, 35, 2111–2122.

Stevens, B. (2006) Bulk boundary-layer concepts for simplified models of tropical dynamics. *Theoretical and Computational Fluid Dynamics*, 20, 279–304. https://doi.org/10.1007/s00162-006-0032-z.

Stevens, B., Cotton, W.R., Feingold, G. and Moeng, C.-H. (1998) Large-eddy simulations of strongly precipitating, shallow, stratocumulus-topped boundary layers. *Journal of the Atmospheric Sciences*, 55, 3616–3638.

Stevens, B., Moeng, C.H. and Sullivan, P.P. (1999) Large-eddy simulation of radiatively driven convection: sensitivities to the representation of small scales. *Journal of the Atmospheric Sciences*, 56, 3963–3984.

Stevens, B., Lenschow, D.H., Faloona, I., Moeng, C.-H., Lilly, D.K., Blomquist, B., Vali, G., Bandy, A., Campos, T., Gerber, H., Haimov, S., Morley, B. and Thornton, D. (2003) On entrainment rates in nocturnal marine stratocumulus. *Quarterly Journal of the Royal Meteorological Society*, 129, 3469–3493.

Stevens, B., Moeng, C.-H., Ackerman, A.S., Bretherton, C.S., Chlond, A., de Roode, S., Edwards, J., Golaz, J.C., Jiang, H., Khairoutdinov, M. and Kirkpatrick, M.P. (2005) Evaluation of large-eddy simulations via observations of nocturnal marine stratocumulus. *Monthly Weather Review*, 133, 1443–1462.

Tellado, P.A. (2013) *Physical processes in coastal stratocumulus clouds from aircraft measurements during UPPEF 2012*. MS Thesis, Monterey, CA: Naval Postgraduate School..

Turton, J.D. and Nicholls, S. (1987) A study of the diurnal variation of stratocumulus using a multiple mixed layer model. *Quarterly Journal of the Royal Meteorological Society*, 113, 969–1009.

Van der Dussen, J.J., de Roode, S.R. and Siebesma, A.P. (2014) Factors controlling rapid stratocumulus cloud thinning. *Journal of the Atmospheric Sciences*, 71, 655–664.

Van der Dussen, J.J., de Roode, S.R. and Siebesma, A.P. (2016) How large-scale subsidence affects stratocumulus transitions. *Atmospheric Chemistry and Physics*, 16, 691–701.

VanZanten, M.C., Duynkerke, P. and Cuijpers, J. (1999) Entrainment parametrization in convective boundary layers. *Journal of the Atmospheric Sciences*, 56, 813–828.

Wang, Q., Tellado, P., Khelif, D., Nielsen, K., Jonsson, H. and Bucholtz, A. (2014) *UPPEF flight summaries for CIRPAS Twin Otter measurements*. Available at: http://met.nps.edu/~qwang/UPPEF/.

Wang, S., Golaz, J.C. and Wang, Q. (2008) Effect of intense wind shear across the inversion on stratocumulus clouds. *Geophysical Research Letters*, 35, L15814. https://doi.org/10.1029/2008GL033865.

Wood, R. (2007) Cancellation of aerosol indirect effects in marine stratocumulus through cloud thinning. *Journal of the Atmospheric Sciences*, 64, 2657–2669.

Wood, R. (2012) Stratocumulus clouds. *Monthly Weather Review*, 140, 2373–2423.

Wyant, M.C., Bretherton, C.S., Rand, H.A. and Stevens, D.E. (1997) Numerical simulations and a conceptual model of the stratocumulus to trade cumulus transition. *Journal of the Atmospheric Sciences*, 54, 168–192.

Yamaguchi, T. and Randall, D.A. (2008) Large-eddy simulation of evaporatively driven entrainment in cloud-topped mixed layers. *Journal of the Atmospheric Sciences*, 65, 1481–1504.

Yamaguchi, T., Randall, D.A. and Khairoutdinov, M.F. (2011) Cloud modeling tests of the ultimate-macho scalar advection scheme. *Monthly Weather Review*, 139, 3248–3264.

Zhu, P., Bretherton, C.S., Kohler, M., Chen, A., Chlond, A., Geng, Q., Austin, P.H., Golaz, J.-C., Lenderink, G., Lock, A. and Stevens, B. (2005) Intercomparison and interpretation of single-column model simulations of a nocturnal stratocumulus topped marine boundary layer. *Monthly Weather Review*, 133, 2741–2758.
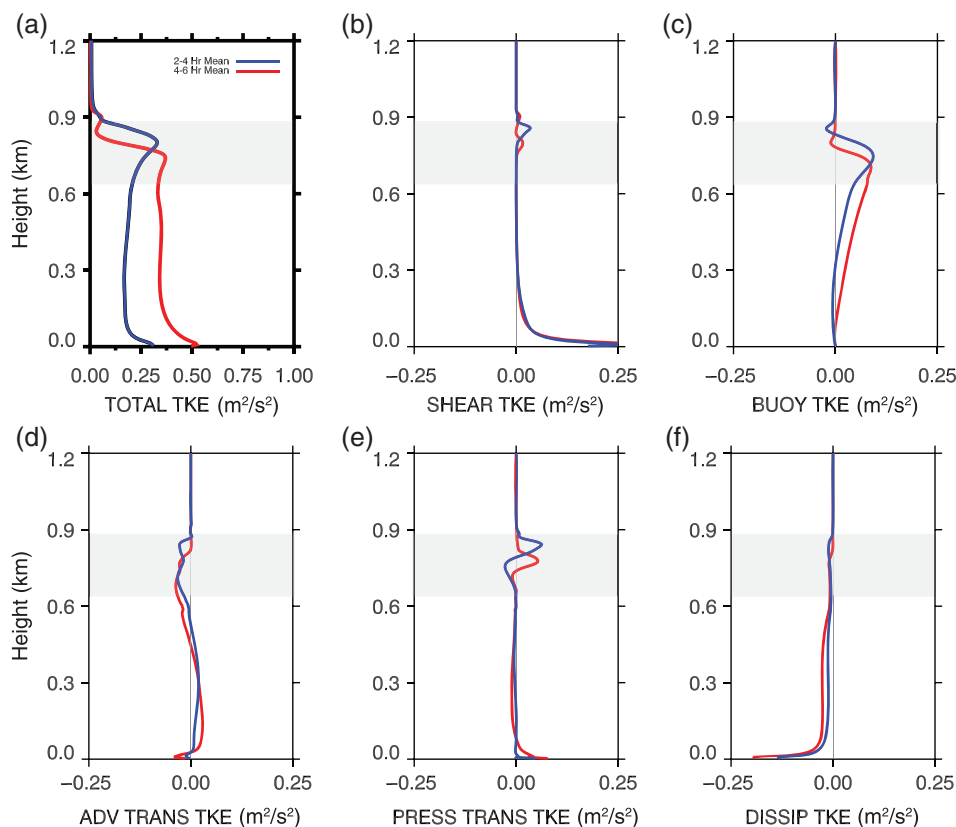
APPENDIX

FIGURE A1 TKE budget profiles for 2–4 and 4–6-hour periods. Total TKE = Shear production of TKE + buoyant production of TKE + advective transport of TKE + pressure transport of TKE + TKE dissipation.